Inter-comparison and improvement of two-stream shortwave radiative transfer models in ESMs for a unified treatment of cryospheric surfaces

Cheng Dang[1], Charles S. Zender[1], Mark G. Flanner[2]

[1] Department of Earth System Science, University of California, Irvine, CA, USA

[2] Department of Climate and Space Sciences and Engineering, University of Michigan, Ann Arbor, MI, USA

Correspondence to: Cheng Dang (cdang5@uci.edu)

Abstract. Snow is an important climate regulator because it greatly increases the surface albedo of large parts of the Earth. Earth System Models (ESMs) often adopt two-stream approximations with different radiative transfer techniques, the same snow therefore has different solar radiative properties depending whether it is on land or on sea ice. Here we inter-compare three two-stream algorithms widely used in snow models, improve their predictions at large zenith angles, and introduce a hybrid model suitable for all cryospheric surfaces in ESMs. The algorithms are those employed by the SNow ICe and Aerosol Radiative (SNICAR) module used in land models, and by dEdd-AD used in Icepack, the column physics used in the Los Alamos sea ice model CICE and MPAS-seaice, and a two-stream discrete ordinate (2SD) model. Compared with a 16-stream benchmark model, the errors in snow visible albedo for a direct-incident beam from all three two-stream models are small ($<\pm0.005$) and increase as snow shallows, especially for aged snow. The errors in direct near-infrared (near-IR) albedo are small ($<\pm0.005$) for solar zenith angles $\theta < 75°$, and increase as θ increases. For diffuse incidence under cloudy skies, dEdd-AD produces the most accurate snow albedo for both visible and near-IR ($<\pm0.0002$) with the lowest underestimate (-0.01) for melting thin snow. SNICAR performs similarly to dEdd-AD for visible albedos, with a slightly larger underestimate (-0.02), while it overestimates the near-IR albedo by an order of magnitude more (up to 0.04). 2SD overestimates both visible and near-IR albedo by up to 0.03. We develop a new parameterization that adjusts the underestimated direct near-IR albedo and overestimated direct near-IR heating persistent across all two-stream models for solar zenith angles > 75°. These results are incorporated in a hybrid model SNICAR-AD, which can now serve as a unified solar radiative transfer model for snow in ESM land, land ice, and sea-ice components.

1. Introduction

Snow cover on land, land ice, and sea ice, modulates the surface energy balance of mid and high latitudes of the Earth, principally because even a thin layer of snow can greatly increase the surface albedo. Integrated over the solar spectrum, the broadband albedo of opaque snow ranges from 0.7 – 0.9 (e.g., Wiscombe and Warren 1980; Dang et al., 2015). In contrast, the albedo of other natural surfaces is smaller: 0.2, 0.25, and 0.5-0.7 for damp soil, grassland, and bare multi-year sea ice, respectively (Perovich 1996; Liang et al., 2002; Brandt et al., 2005; Bøggild et al., 2010). The accumulation, evolution, and depletion of snow cover modify the seasonal cycle of surface albedo globally. In particular, snow over sea ice absorbs more solar energy and begins to melt in the spring, which forms melt ponds that bring the sea-ice albedo to as low as 0.15 to further accelerate ice melt (Light et al., 2008, 2015). An accurate simulation of the shortwave radiative properties of snowpack is therefore crucial for spectrally partitioning solar energy and representing snow-albedo feedbacks across the Earth system. Unfortunately, computational demands and coupling architectures often constrain representation of snowpack radiative processes in Earth System Models (ESMs, please refer to Table 1 for all acronyms used in this work) to relatively crude approximations such as two-stream methods (Wiscombe and Warren, 1980, Toon et al., 1989). In this work, we inter-compare two-stream methods widely used in snow models and then introduce a new parameterization that significantly reduces their snowpack reflectance and heating biases at large zenith angles, to produce more realistic behavior in polar regions.

Snow albedo is determined by many factors including the snow grain radius, the solar zenith angle, cloud transmittance, light-absorbing particles, and the albedo of underlying ground if snow is optically thin (Wiscombe and Warren, 1980; Warren and Wiscombe, 1980); it also varies strongly with wavelength since the ice absorption coefficient varies by 7 orders of magnitudes across the solar spectrum (Warren and Brandt, 2008). At visible wavelengths (0.2 - 0.7 μm), ice is almost non-absorptive such that the absorption of visible energy by snowpack is mostly due to the light-absorbing particles (e.g. black carbon, organic carbon, mineral dust) that were incorporated during ice nucleation in clouds, scavenged during precipitation, or slowly sedimented from the atmosphere by gravity (Warren and Wiscombe, 1980, 1985; Doherty et al., 2010, 2014, 2016; Wang et al., 2013; Dang and Hegg 2014). As snow becomes shallower, visible photons are more likely to penetrate through snowpack and get absorbed by darker underlying ground. At near-infrared (near-IR) wavelengths (0.7 – 5 μm), ice is much more absorptive that the

72 snow albedo is lower than the visible albedo. Larger ice crystals form a lower albedo

73 surface than smaller ice crystals hence aged snowpacks absorb more solar energy.

74 Photons incident at smaller solar zenith angles are more likely to penetrate deeper

75 vertically and be scattered in the snowpack until being absorbed by the ice/the underlying

76 ground/absorbing impurities, which also leads to a smaller snow albedo. To compute the

77 reflected solar flux, spectrally resolved albedo must be weighted by the incident solar

78 flux, which is mostly determined by solar zenith angle, cloud cover and transmittance,

79 and column water vapor. Modeling the solar properties of snowpacks must consider the

80 spectral signatures of these atmospheric properties.

81

82 Several parameterizations have been developed to compute the snow solar properties

83 without solving the radiative transfer equations and some are incorporated into ESMs or

84 regional models. Marshall and Warren (1987) and Marshall (1989) parameterized snow

85 albedo in both visible and near-IR bands as functions of snow grain size, solar zenith

86 angle, cloud transmittance, snow depth, underlying surface albedo, and black carbon

87 content. Marshall and Oglesby (1994) used this in an ESM. Gardner and Sharp (2010)

88 parameterized the all-wave snow albedo with similar inputs. This was incorporated into

89 the regional climate model RACMO

90 (https://www.projects.science.uu.nl/iceclimate/models/racmo.php) to simulate snow

91 albedo in glaciered regions like Antarctica and Greenland (Munneke et al., 2011). Dang

92 et al., (2015) compute snow albedo as functions of snow grain radius, black carbon

93 content, and dust content for visible and near-IR bands and 14 narrower bands used in the

94 rapid radiative transfer model (RRTM, Mlawer and Clough, 1997). Their

95 parameterization can also be expanded to different solar zenith angles using the zenith

96 angle parameterization developed by Marshall and Warren (1987). Aoki et al., (2011)

97 developed a more complex model based on the offline snow albedo and a transmittance

98 look-up table. This can be applied to multilayer snowpack to compute the snow albedo

99 and the solar heating profiles as functions of snow grain size, black carbon and dust

100 content, snow temperature, and snowmelt water equivalent. These parameterizations are

101 often in the form of simplified polynomial equations, which are especially suitable to

102 long-term ESM simulations that require less time-consuming snow representations.

103

104 More complex models that explicitly solve the multiple scattering radiative transfer

105 equations have also been developed to compute snow solar properties. Flanner and

106 Zender (2005) developed the SNow Ice and Aerosol Radiation model (SNICAR) that

107 utilizes two-stream approximations (Wiscombe and Warren 1980; Toon et al., 1989) to

108   predict heating and reflectance for multi-layer snowpack. They implemented SNICAR in
109   the Community Land Model (CLM) to predict snow albedo and vertically-resolved solar
110   absorption for snow-covered surfaces. Before SNICAR, CLM prescribed snow albedo
111   and confined all solar absorption to the top snow layer (Flanner and Zender 2005). Over
112   the past decades, updates and new features have been added to SNICAR to consider more
113   processes such as black carbon/ice mixing states (Flanner et al., 2012) and snow grain
114   shape (He et al., 2018b). Concurrent with the development of SNICAR, Briegleb and
115   Light (2007) improved the treatment of sea-ice solar radiative calculations in Community
116   Climate System Model (CCSM). They implemented a different two-stream scheme with
117   delta-Eddington approximation and adding-doubling technique (hereafter, dEdd-AD) that
118   allows CCSM to compute bare/ponded/snow-covered sea ice albedo and solar absorption
119   profiles of multi-layer sea ice. Before these improvements, the sea-ice albedo was
120   computed based on surface temperature, snow thickness, and sea-ice thickness using
121   averaged sea ice and snow albedo. dEdd-AD has been adopted by the sea-ice physics
122   library Icepack (https://github.com/CICE-Consortium/Icepack/wiki), which is used by the
123   Los Almos Sea Ice Model CICE (Hunke et al., 2010) and Model for Prediction Across
124   Scales Sea Ice MPAS-seaice (Turner et al., 2018). CICE itself is used in numerous global
125   and regional models.
126
127   SNICAR and dEdd-AD solve the multiple scattering radiative transfer equations and
128   provide much improved solar radiative representations for the cryosphere, though their
129   separate development and implementation created an artificial divide for snow
130   simulation. In ESMs that utilize both SNICAR and dEdd-AD, such as the Community
131   Earth System Model (CESM, http://www.cesm.ucar.edu/) and the Energy Exscale Earth
132   System Model (E3SM, previously known as ACME, https://e3sm.org/), the solar
133   radiative properties of snow on land and snow on sea ice are computed separately via
134   SNICAR and dEdd-AD. As a result, the same snow in nature has different solar radiative
135   properties such as reflectance depending on which model represents it. These differences
136   are model artifacts that should be eliminated so that snow has consistent properties across
137   the Earth system.
138
139   In this paper, we evaluate the accuracy and biases of three two-stream models listed in
140   Table 2, including the algorithms used in SNICAR and dEdd-AD, at representing
141   reflectance and heating. In Sections 2-4, we describe the radiative transfer algorithms and
142   calculations performed in this work. The results and model inter-comparisons are
143   discussed in Section 5. In Section 6, we introduce a parameterization to reduce the

144   simulated albedo and heating bias for solar zenith angles larger than 75°. In Section 7, we

145   summarize the major differences of algorithm implementations between SNICAR and

146   dEdd-AD in ESMs. We use these results to develop and justify a unified surface

147   shortwave radiative transfer method for all Earth system model components in the

148   cryosphere, presented in Section 8.

149

150   **2. Radiative Transfer Model**

151

152   In this section, we summarize the three two-stream models and the benchmark DISORT

153   model with 16-streams. These algorithms are well documented in papers by Toon et al.,

154   (1989), Briegleb and Light (2007), Jin and Stamnes (1994), and Stamnes et al. (1988).

155   Readers interested in detailed mathematical derivations should refer to those papers. We

156   only include their key equations to illustrate the difference among two-stream models for

157   discussion purposes.

158

159   2.1 SNICAR in land models CLM and ELM

160   SNICAR is implemented as the default snow shortwave radiative transfer scheme in

161   CLM and E3SM land model (ELM). It adopts the two-stream algorithms and the rapid

162   solver developed by Toon et al., (1989) to compute the solar properties of multi-layer

163   snowpacks. These two-stream algorithms are derived from the general equation of

164   radiative transfer in a plane parallel media:

165

166    $\mu \frac{\partial I}{\partial \tau}(\tau, \mu, \Phi) = I(\tau, \mu, \Phi) - \frac{\varpi}{4\pi} \int_0^{2\pi} \int_{-1}^{1} P(\mu, \mu', \phi, \phi') \, I(\tau, \mu', \Phi') d\mu' d\phi' - S(\tau, \mu, \Phi)$

167

168   (1)

169

170

171   where arccos(μ) and Φ are zenith angle and azimuth angle, ϖ is single-scattering albedo.

172   On the right-hand side, the three terms are intensity at optical depth τ, internal source

173   term due to multiple scattering, and external source term S. For a purely external source

174   at solar wavelengths S is:

175

176    $S = \frac{\varpi}{4} F_s P(\mu, -\mu_0, \phi, \phi_0) exp\left(\frac{-\tau}{\mu_0}\right)$ (2)

177

178   where πF_s is incident solar flux, μ_0 is the incident direction of the solar beam. Integrating

179   equation (1) over azimuth and zenith angles yields the general solution of two-stream

180 approximations (Meador and Weaver, 1980). The upward and downward fluxes at optical
181 depth τ of layer n can be represented as:

$$F_n^+ = k_{1n} \, exp(\Lambda_n\tau) + \Gamma_n k_{2n} \, exp(-\Lambda_n\tau) + C_n^+(\tau) \tag{3a}$$

$$F_n^- = \Gamma_n k_{1n} \, exp(\Lambda_n\tau) + k_{2n} \, exp(-\Lambda_n\tau) + C_n^-(\tau) \tag{3b}$$

189 where Λ_n, Γ_n C_n are known coefficients determined by the two-stream method, incident

190 solar flux, and solar zenith angle; whereas k_{1n} and k_{2n} are unknown coefficients

191 determined by the boundary conditions. For an N-layer snowpack, the solutions for

192 upward and downward fluxes are coupled at layer interfaces to generate 2N equations

193 with 2N unknown coefficients k_{1n} and k_{2n}. Combining these equations linearly generates

194 a new set of equations with terms in tridiagonal form that enables the application of a fast

195 tri-diagonal matrix solver. With the solved coefficients, the upward and downward fluxes

196 are computed at different optical depths (Equations 3a and 3b) and eventually the

197 reflectance, transmittance, and absorption profiles of solar flux for any multilayer

198 snowpack.

200 SNICAR itself implements all three two-stream algorithms in Toon et al., (1989):

201 Eddington, Quadrature, and Hemispheric-mean. In practical simulations, it utilizes the

202 Eddington and Hemispheric-mean approximations to compute the visible and near-IR

203 snow properties, respectively (Flanner et al., 2007). In addition to their algorithms,

204 SNICAR implements the Delta-transform of the fundamental input variables asymmetry

205 factor (g), single-scattering albedo (ϖ), and optical depth (τ) to account for the strong

206 forward scattering in snow (Equations 2 (a)-(c), Wiscombe and Warren, 1980).

208 2.2. dEdd-AD in sea ice models Icepack, CICE, and MPAS-seaice

209 Icepack, CICE, and MPAS-seaice use the same shortwave radiative scheme dEdd-AD

210 developed and documented by Briegleb and Light (2007). Sea ice is divided into multiple

211 layers to first compute the single-layer reflectance and transmittance using two-stream

212 delta-Eddington solutions to account for the multiple scattering of light within each layer

213 (Equation set 50, Briegleb and Light, 2007), where the name "delta" implies dEdd-AD

214 implements the Delta-transform to account for the strong forward scattering of snow and

215 sea ice (Equations 2 (a)-(c), Wiscombe and Warren, 1980). The single-layer direct albedo
216 and transmittance are computed by equations:

217

218 $$R(\mu_{0,n}) = A_n \, exp\left(\frac{-\tau}{\mu_{0,n}}\right) + B_n(exp(\varepsilon_n\tau) - exp(-\varepsilon_n\tau)) - K_n \tag{4a}$$

219

220 $$T(\mu_{0,n}) = E_n + H_n(exp(\varepsilon_n\tau) - exp(-\varepsilon_n\tau)) \, exp\left(\frac{-\tau}{\mu_{0,n}}\right) \tag{4b}$$

221
222 where coefficients A_n, B_n, K_n, E_n, H_n, and ε_n are determined by the single-scattering
223 albedo (ϖ), asymmetry factor (g), optical depth (τ), and angle of the incident beam at
224 layer n ($\mu_{0,n}$). Following the delta-Eddington assumption, simple formulas are available
225 for the single-layer reflectance and transmittance under both clear sky (direct flux,
226 equations 4a and 4b) and overcast sky (diffuse flux) conditions, however, the formula
227 derived by applying diffuse-flux upper boundary conditions sometimes yields negative
228 albedos (Wiscombe 1977). To avoid the unphysical values, diffuse reflectance $\bar{R}$ and
229 transmittance $\bar{T}$ of a single layer are computed by integrating the direct reflectance $R(\mu)$
230 and transmittance $T(\mu)$ over the incident hemisphere assuming isotropic incidence:

231

232 $$\bar{R} = 2 \int_0^1 \mu R(\mu) d\mu \tag{5a}$$

233
234 $$\bar{T} = 2 \int_0^1 \mu T(\mu) d\mu \tag{5b}$$

235

236 This is the same as the method proposed by Wiscombe and Warren (1980, their equation
237 5). In practice, eight Gaussian angles are implemented to perform the integration for
238 every layer.

239

240 The computed single-layer reflectance and transmittance of direct and diffuse
241 components are then combined to account for the inter-layer scattering of light to
242 compute the reflectance and transmission at every interface (Equation set 51, Briegleb
243 and Light, 2007), and eventually the upward and downward fluxes (Equation set 52,
244 Briegleb and Light, 2007). These upward and downward fluxes at each optical depth are
245 then used to compute the column reflectance and transmittance, and the absorption
246 profiles for any multilayered media, such as snowpacks on land and sea ice.

247

248 In nature, a large fraction of sea ice is covered by snow during winter. As snow melts
249 away in late spring and summer, it exposes bare ice, and melt ponds form on the ice

250   surface. Such variation of sea-ice surface types requires the shortwave radiative transfer

251   model to be flexible and capable of capturing the light refraction and reflection.

252   Refractive boundaries exist where air (refractive index m_{re} = 1.0), snow (assuming snow

253   as medium of air containing a collection of ice particles, m_{re} = 1.0), pond (assuming pure

254   water, m_{re} = 1.33), and ice (assuming pure ice, m_{re} = 1.31) are present in the same sea-ice

255   column. The general solution of delta-Eddington, and the two-stream algorithms used in

256   SNICAR are not applicable to such non-uniformly refractive layered media. To include

257   the effects of refraction, Briegleb and Light (2007) modified the adding formula at the

258   refractive boundaries (i.e. interfaces between air/ice, snow/ice, air/pond). The reflectance

259   and transmittance of the adjacent layers above and below the refractive boundary are

260   combined with modifications to include the Fresnel reflection and refraction of direct and

261   diffuse fluxes (Section 4.1, Briegleb and Light, 2007). dEdd-AD can thus be applied to

262   any layered media with either uniform (e.g., snow on land) or non-uniform (e.g., snow on

263   sea ice) refractive indexes.

264

265   In this paper, we apply dEdd-AD to snowpacks that can be treated as uniform refractive

266   media such as the air/snowpack/land columns assumed in SNICAR for model evaluation.

267   An ideal radiative treatment for snow should, however, keep the potential to include

268   refraction for further applications to snow on sea ice or ice sheets. Therefore, besides

269   these two widely used algorithms in Icepack and SNICAR, we evaluate a third algorithm

270   (section 2.3) that can be applied to layered media with either uniform or non-uniform

271   refractive indexes.

272

273   2.3. two-stream discrete-ordinate algorithm (2SD)

274   A refractive boundary also exists between the atmosphere and the ocean, and models

275   have been developed to solve the radiative transfer problems in the atmosphere-ocean

276   system using the discrete-ordinate technique (e.g. Jin and Stamnes, 1994; Lee and Liou,

277   2007). Similar to the two-stream algorithms of Toon et al., (1989) used in SNICAR, Jin

278   and Stamnes (1994) also developed their algorithm from the general equation:

279

280   $\mu \frac{\partial I}{\partial \tau}(\tau, \mu) = I(\tau, \mu) - \frac{\varpi}{4\pi} \int_{-1}^{1} P(\tau, \mu, \mu') I(\tau, \mu') d\mu' - S(\tau, \mu)$ (6)

281

282   Equation (6) is the azimuthally integrated version of equation (1). However, for vertically

283   inhomogeneous media like the atmosphere-ocean or sea ice, the external source term

284   $S(\tau, \mu)$ is different. Specifically, for the medium of total optical depth τ^a above the

285 refractive interface, one must consider the contribution from the upward beam reflected
286 at the refractive boundary (second term on the right-hand side):
287

288 $$S^a(\tau, \mu) = \frac{\varpi}{4\pi} F_s P(\tau, -\mu_0, \mu) \, exp\left(\frac{-\tau}{\mu_0}\right) + \frac{\varpi}{4\pi} F_s R(-\mu_0, m) P(\tau, +\mu_0, \mu) exp\left(\frac{-(2\tau^a - \tau)}{\mu_0}\right)$$
289

290 $$(7)$$
291

292 where $R(-\mu_0, m)$ is the Fresnel reflectance of radiation and m is the ratio of the
293 refractive indices of the lower to the upper medium. For the medium below the refractive
294 interface, one must account for the Fresnel transmittance $T(-\mu_0, m)$ and modify the
295 angle of beam travel in media b:
296

297 $$S^b(\tau, \mu) = \frac{\varpi}{4\pi} \frac{\mu_0}{\mu_{0n}} F_s T(-\mu_0, m) P(\tau, -\mu_0, \mu) \, exp\left(\frac{-\tau^a}{\mu_0}\right) exp\left(\frac{-(\tau - \tau^a)}{\mu_{0n}}\right) \qquad (8)$$
298

299 where μ_{0n} is the cosine zenith angle of refracted beam incident at angle μ_0 above the
300 refractive boundary, by Snell's law:
301

302 $$\mu_{0n} = \sqrt{1 - (1 - \mu_0^2)/m^2} \qquad (9)$$
303

304 For uniformly refractive media like snow on land, one can just set the refractive index m_{re}
305 equal to 1 for every layer. In this case, the Fresnel reflectance $R(-\mu_0, m)$ is 0 in equation
306 (7), the Fresenal transmittance $T(-\mu_0, m)$ is 1 in equation (8), and μ_{0n} equals to μ_0: the
307 two source terms $S^a(\tau, \mu)$ and $S^b(\tau, \mu)$ become the same and equal to the source term of
308 homogenous media given in equation (2).
309

310 For two-stream approximations of this method, analytical solutions of upward and
311 downward fluxes are coupled at each layer interface to generate 2N equations with 2N
312 unknown coefficients for any N-layer stratified column. The solutions of two-stream
313 algorithms and boundary conditions for homogenous media are well documented
314 (Sections 8.4 and 8.10 of Thomas and Stamnes, 1999). Despite the extra source terms,
315 these 2N equations can also be organized into a tridiagonal matrix similar to the method
316 of Toon et al. (1989) used in SNICAR. Flexibility and speed therefore make this two-
317 stream discrete-ordinate algorithm (hereafter, 2SD) a potentially good candidate for long-

318   term Earth system modeling. In this work, we only apply 2SD to snowpack and note that
319   it can be applied to any uniformly or non-uniformly refractive media like snow on land or
320   sea ice, with the Delta-transform implemented to fundamental optical variables
321   (Equations 2 (a)-(c), Wiscombe and Warren, 1980).
322
323   2.4 16-stream DISORT
324   Besides the mathematical technique, the accuracy and speed of radiative transfer
325   algorithms depend on the number of angles used for flux estimation in the upward and
326   downward hemispheres. SNICAR, dEdd-AD, and 2SD use one angle to represent upward
327   flux and one angle to represent downward flux, hence they are named two-stream
328   algorithm. Lee and Liou (2007) use two upward and two downward streams. Jin and
329   Stamnes (1994) documented the solutions for any even number of streams. The
330   computational efficiency of these models is lower than that of two-stream models while
331   their accuracy is better. To quantify the accuracy of the three two-stream algorithms for
332   snow shortwave simulations, we use the 16-stream DIScrete-Odinate Radiative Transfer
333   model (DISORT) as the benchmark model (http://lllab.phy.stevens.edu/disort/) (Stamnes
334   et al., 1988).
335
336   **3. Input for radiative transfer models**
337   In this work, we focus on the performance of two-stream algorithms for pure snow
338   simulations. The inputs for these three models are the same: single-scattering properties
339   (SSPs, i.e. single-scattering albedo ϖ, asymmetry factor g, extinction coefficient σ_{ext}) of
340   snow determined by snow grain radius r, snow depth, solar zenith angle θ, solar incident
341   flux, and the albedo of underlying ground (assuming Lambertian reflectance of 0.25 for
342   all wavelengths). A Delta-transform is applied to fundamental input optical variables for
343   all simulations (Equations 2 (a)-(c), Wiscombe and Warren, 1980).
344
345   In snow, photon scattering occurs at the air-ice interface, and the absorption of photons
346   occurs within the ice crystal. The most important factor that determines snow shortwave
347   properties is the ratio of total surface area to total mass of snow grains, aka "the specific
348   surface area" (e.g. Matzl and Schneebeli, 2006, 2010). The specific surface area (β) can
349   be converted to a radiatively effective snow grain radius r:
350
351   $\beta = 3 / (r \, \varrho_{ice})$ (10)
352

where ρ_{ice} is the density of pure ice, 917 kg m^{-3}. Assuming the grains are spherical, the SSPs of snow can thus be computed using Mie theory (Wiscombe, 1980) and ice optical constants (Warren and Brandt, 2008). In nature, snow grains are not spherical, and many studies have been carried out to quantify the accuracy of such spherical representations (Grenfell and Warren, 1999; Neshyba et al., 2003; Grenfell et al., 2005). In recent years, more research has been done to evaluate the impact of grain shape on snow shortwave properties (Dang et al., 2016; He et al., 2017, 2018ab), and they show that non-spherical snow grain shapes mainly alter the asymmetry factor. Dang et al., (2016) also point out that the solar properties of a snowpack consisting of non-spherical ice grains can be mimicked by a snowpack consisting of spherical grains with a smaller grain size by factors up to 2.4. In this work, we still assume the snow grains are spherical, and this assumption does not qualitatively alter our evaluation of the radiative transfer algorithms.

The input SSPs of snow grains are computed using Mie theory at a fine spectral resolution for a wide range of ice effective radius r from 10 to 3000 μm that covers the possible range of grain radius for snow on Earth (Flanner et al., 2007). The same spectral SSPs were also used to derive the band-averaged SSPs of snow used in SNICAR. Note Briegleb and Light (2007) refer to SSPs as inherent optical properties.

4. Solar spectra used for the spectral integrations

In climate modeling, snow albedo computation at a fine spectral resolution is expensive and unnecessary. Instead of computing spectrally resolved snow albedo as shown in Figure 1, wider-band solar properties are more practical. For example, CESM and E3SM aggregate the narrow RRTMG bands used for the atmospheric radiative transfer simulation into visible (0.2 - 0.7 μm) and near-IR (0.7 - 5 μm) bands. The land model and sea-ice model thus receive visible and near-IR fluxes as the upper boundary condition, and return the corresponding visible and near-IR albedos to atmosphere model. In practice, these bands are also partitioned into direct and diffuse components. Therefore, a practical two-stream algorithm should be able to simulate the direct visible, diffuse visible, direct near-IR and diffuse near-IR albedos and absorptions of snow accurately.

The band albedo α is an irradiance-weighted average of the spectral albedo $\alpha(\lambda)$:

$$\alpha = \frac{\int_{\lambda 1}^{\lambda 2} \alpha(\lambda)F(\lambda)d\lambda}{\int_{\lambda 1}^{\lambda 2} F(\lambda)d\lambda} \tag{11}$$

389   In this work, we use the spectral irradiance $F(\lambda)$ generated by the atmospheric DISORT-
390   based Shortwave Narrowband Model (SWNB2) (Zender et al., 1997; Zender, 1999) for
391   typical clear-sky and cloudy-sky conditions of mid-latitude winter as shown in Figure
392   2(a). The total clear-sky down-welling surface flux at different solar zenith angles are
393   also given in Figure 2(b).
394
395
396   **5. Model Evaluation**
397   5.1 Spectral albedo and reflected solar flux
398   The spectral reflectance of pure deep snow computed using two-stream models and 16-
399   stream DISORT are shown in Figure 1. The snow grain radius is 100 μm - a typical grain
400   size for fresh new snow. For clear sky with direct beam source (left column), all three
401   two-stream models show good accuracy at visible wavelengths (0.3 – 0.7 μm), and within
402   this band, the snow albedo is large and close to 1. As wavelength increases, the albedo
403   diminishes in the near-IR band. two-stream models overestimate snow albedo at these
404   wavelengths, with maximum biases of 0.013 (SNICAR and dEdd-AD) and 0.023 (2SD)
405   within wavelength 1 - 1.7 μm. For cloudy-sky cases with diffuse upper boundary
406   conditions, dEdd-AD reproduces the snow albedo at all wavelengths with the smallest
407   absolute error (< 0.005), SNICAR and 2SD both overestimate the snow albedo with
408   maximum biases > 0.04 between 1.1-1.4 μm.
409
410   In both sky conditions, the errors of snow albedo are larger at near-IR wavelengths
411   ranging from 1.0-1.7 μm, while the solar incident flux peaks at 0.5 μm then decrease as
412   wavelength increases. The largest error in reflected flux is within the 0.7-1.5 μm band for
413   SNICAR and 2SD, as shown in the 3rd row of Figure 1. dEdd-AD overestimate the direct
414   snow albedo mostly at wavelengths larger than 1.5 μm where the error in reflected flux is
415   almost negligible.
416
417   5.2 Broadband albedo and reflected solar flux
418   Integrated over the visible and near-IR wavelengths, the error in band albedos computed
419   using two-stream models for different cases are shown in Figure 3-6.
420
421   Figure 3 shows the error in direct band albedo for fixed snow grain radius of 100 μm with
422   different snow depth and solar zenith angles. As introduced in Section 2, SNICAR and
423   dEdd-AD both use delta-Eddington method to compute the visible albedo. They
424   overestimate the visible albedo for solar zenith angles smaller than 50° by up to 0.005,

425 and underestimate it for solar zenith angles larger than 50° by up to -0.01. 2SD produces
426 similar results for the visible band but at a larger solar zenith angle threshold of 75°. In
427 the near-IR band, SNICAR and 2SD overestimate the snow albedo for solar zenith angles
428 smaller than 70°, beyond this, the error in albedo increases by up to -0.1 as solar zenith
429 angle increases. dEdd-AD produces a similar error pattern with a smaller solar zenith
430 angle threshold at 60°. As snow ages, its average grain size increases. For typical old
431 melting snow of grain radius 1000 μm (Figure 4), two-stream models produce similar
432 errors of direct albedo in all bands. For snow consisting of smaller grain size, two-stream
433 models produce larger errors for visible albedo. Integrating over the entire solar band, the
434 three two-stream models evaluated show similar error patterns for direct albedo.
435
436 For a fixed solar zenith angle of 60°, the error of direct albedo for different snow depth
437 and snow grain radii are shown in Figure 5. SNICAR and dEdd-AD underestimate the
438 visible albedo in most scenarios, while 2SD overestimates the visible albedo for a larger
439 range of grain radius and snow depth. All three two-stream models tend to overestimate
440 the near-IR albedo except for shallow snow with large grain radius; the error of 2SD is
441 one order of magnitude larger than that of SNICAR and dEdd-AD.
442
443 Figure 6 is similar to Figure 5, but shows the diffuse snow albedo. In the visible band,
444 SNICAR and dEdd-AD generate similar errors in that they both underestimate the albedo
445 as snow grain size increases and snow depth decreases. 2SD overestimates the albedo
446 with a maximum error of around 0.015. In the near-IR, two-stream models tend to
447 overestimate snow albedo, while the magnitude of biases produced by SNICAR and 2SD
448 are one order larger than that of dEdd-AD with the maximum error of 0.035 generated by
449 SNICAR. As a result, the all-wave diffuse albedos computed using dEdd-AD are more
450 accurate than those computed using SNICAR and 2SD.
451
452 Figures 7, 8 and 9 show the errors in reflected shortwave flux caused by snow albedo
453 errors seen in Figures 3, 4, and 6. In general, two-stream models produce larger errors in
454 reflected direct near-IR flux (Figure 7 and 8), especially with the 2SD model: the
455 maximum overestimate of reflected near-IR flux is 6-8 Wm^{-2} for deep melting snow with
456 solar zenith angle < 30°. Errors in reflected direct visible flux are smaller (mostly within
457 ±1 Wm^{-2}) for all models in most scenarios, and become larger (mostly within ±3 Wm^{-2}) as
458 snow grain size increases to 1000 μm if computed using 2SD. As shown in Figure 9, for
459 diffuse flux with solar zenith angle of 60° at TOA, SNICAR and dEdd-AD generate

460   small errors in reflected visible flux (mostly within ±1 Wm^{-2}), while 2SD always

461   overestimates reflected visible flux by up to 5 Wm^{-2}. In the near-IR, SNICAR and 2SD

462   overestimate reflected flux by as much as 10-12 Wm^{-2}; the error in reflected near-IR flux

463   produced by dEdd-AD is much smaller, mostly within ±1 Wm^{-2}.

464

465   In general, dEdd-AD produces the most accurate albedo and thus reflected flux for both

466   direct and diffuse components. SNICAR is similar to dEdd-AD for its accuracy of direct

467   albedo and flux, yet generates large error for the diffuse component. 2SD tends to

468   overestimate snow albedo and reflected flux in both direct and diffuse components and

469   shows the largest errors among three two-stream models. These relatively small

470   differences between algorithms may still yield large impact on snowpack. For example,

471   compared to dEdd-AD, SNICAR and 2SD overestimate the diffuse albedo by ~0.015 for

472   melting snow (Figure 6). In Greenland, the daily averaged downward diffuse solar flux

473   from May to September is 200 W/m^2, and the averaged cloud cover fraction is 80%

474   (Figure 6, Dang et al., 2017). In this case, SNICAR and 2SD overestimate the reflected

475   solar flux by 2.4 W/m^2 per day – the amount of energy otherwise enough to melt 10 cm of

476   snow water equivalent from May to September. dEdd-AD also remediates self-

477   compensating spectral biases (where visible and Near-IR biases are of opposite signs)

478   present in the other schemes. Those spectral biases do not affect the broadband fluxes

479   like the diffuse biases, but they nevertheless degrade proper feedbacks between snow/ice

480   reflectance and heating."

481

482   5.3 Band absorption of solar flux

483   Figure 10 shows absorption profiles of shortwave flux computed using the 16-stream

484   DISORT model, with errors in absorbed fractional solar flux computed using two-stream

485   models. The snowpack is 10-cm deep and is divided into 5 layers, each 2-cm thick. The

486   snow grain radius is set to 100 μm. The figure shows fractional absorption for snow

487   layers 1-4 and the underlying ground with an albedo of 0.25.

488

489   As shown in the first column of Figure 10, for new snow with a radius of 100 μm, most

490   solar absorption occurs in the top 2-cm snow layer, where roughly 10% and 15% of

491   diffuse and direct near-IR flux are absorbed and dominate the solar absorption within the

492   snowpack. In the second layer (2-4 cm), the absorption of solar flux is less than 1% and

493   gradually decreases within the interior layers. The underlying ground absorbs roughly 2%

494   of solar flux, mostly visible flux that penetrates the snowpack more efficiently. As snow

ages and snow grain grows, photons penetrate deeper into the snowpack. For typical old melting snow with a radius of 1000 μm, most solar absorption still occurs in the top 2-cm snow layer, where roughly 20% and 14% of diffuse and direct near-IR flux are absorbed. The second snow layer (2-4 cm) absorbs more near-IR solar flux by roughly 2%. More photons can penetrate through the snowpack, and results in a high fractionally absorption by the underlying ground, especially for the visible band. As snow depth increase, the ground absorption will decrease for both snow radii.

Comparing to 16-stream DISORT, two-stream models underestimate (overestimate) the column solar absorptions for new (old) snow, especially for the surface snow layer and the underground. Overall, dEdd-AD gives the most accurate absorption profiles among the three two-stream models, especially for new snow.

6. Correction for direct albedo for large solar zenith angles

It has been pointed out in previous studies that the two-stream approximations become poor as solar zenith angle approaches 90° (e.g. Wiscombe 1977, Warren 1982). As shown in Figures 3 and 4, all three two-stream models underestimate the direct snow albedo for large solar zenith angles. In the visible band, when the snow grain size is small, the error in direct albedo is almost negligible (Figure 3); while as snow ages and snow grains become larger, the error increases yet remains low if the snow is deep (Figure 4). In the near-IR, the biases of albedo are also larger for larger snow grain radii. For a given snow size, the magnitudes of such biases are almost independent of snow depth, and mainly determined by the solar zenith angle. In general, the errors of all-wave direct albedo are mostly contributed by the errors of near-IR albedo, especially for optically thick snowpacks (i.e., semi-infinite), because the errors of direct albedo in the visible are negligible compared with those in the near-IR. To improve the performance of two-stream algorithms, we develop a parameterization that corrects the underestimated near-IR snow albedo at large zenith angles.

Figure 11 shows the direct near-IR albedo and fractional absorption of 2-meter thick snowpacks consisting of grains with radius 100 μm and 1000 μm, computed using two-stream algorithms and 16-stream DISORT. For solar zenith angles > 75°, two-stream models underestimate snow albedo and overestimate solar absorption within snowpack, mostly in the top 2-cm of snow, and the differences among three two-stream models are small. In Section 5, we have shown that dEdd-AD produces the most accurate snow

531   albedo in general, with anticipated wide application of dEdd-AD, we develop the
532   following parameterization to adjust its low biases in computed near-IR direct albedo.
533

534   We define and compute R_{75+} as the ratio of direct semi-infinite near-IR albedo computed
535   using 16-stream DISORT ($\alpha_{16\text{-}DISORT}$) to that computed using dEdd-AD ($\alpha_{dEdd\text{-}AD}$). This
536   ratio is shown in Figure 11 (c) and can be parameterized as a function of snow grain
537   radius (r, unit in meter) and the cosine of incident solar zenith angle (μ_0), as shown in
538   Figure 11(c):
539

540    $$R_{75+} = \frac{\alpha_{16-DISORT}}{\alpha_{dEdd-AD}} = c_1(\mu_0)log_{10}(r) + c_0(\mu_0) \qquad (12)$$
541

542   where coefficients c_1 and c_0 are polynomial functions of μ_0, as shown in Figure 11(d):
543

544    $$c_1(\mu_0) = 1.304\mu_0^2 - 0.631\mu_0 + 0.086 \qquad (13a)$$
545    $$c_0(\mu_0) = 6.807\mu_0^2 - 3.338\mu_0 + 1.467 \qquad (13b)$$
546

547   Since two-stream models always underestimate snow albedo, R_{75+} always exceeds 1
548   (Figure 11c). We can then adjust the direct near-IR snow albedo ($\alpha_{dEdd\text{-}AD}$) and direct
549   near-IR solar absorption ($Fabs_{dEdd\text{-}AD}$) by snow computed using dEdd-AD with ratio
550   R_{75+}:
551

552    $$\alpha_{dEdd-AD}^{adjust} = R_{75+}\alpha_{dEdd-AD} \qquad (14a)$$
553

554    $$Fabs_{dEdd-AD}^{adjust} = Fabs_{dEdd-AD} - (R_{75+} - 1)\alpha_{dEdd-AD}F_{nir} \qquad (14b)$$
555

556   where F_{nir} is the direct near-IR flux. This adjustment reduces the error of near-IR albedo
557   from negative 2-10% to within $\pm$ 0.5% for solar zenith angles larger than 75°, and for
558   grain radii ranging from 30-1500 μm (Figure 12). Errors in broadband direct albedo are
559   therefore also reduced to < 0.01. The direct near-IR flux absorbed by the snowpack
560   decreases after applying this adjustment.
561

562   When the solar zenith angle exceeds 75°, our model adjusts the computed direct near-IR
563   albedo αdEdd-AD by the ratio $R75+$ following equations 12-14a and reduces direct near-

564   IR absorption following equation 14b. If snow is divided into multiple layers, we assume
565   all decreased near-IR absorption (2nd term on the right-hand side, equation 14b) is
566   confined within the top layer. This assumption is fairly accurate for the near-IR band,
567   since most absorption occurs at the surface of snowpack (Figures 10 and 11). As
568   discussed previously, this parameterization is developed based on albedo computed using
569   dEdd-AD. For models that do not use dEdd-AD but SNICAR and 2SD, the same
570   adjustment still applies given the small differences of near-IR direct albedo computed
571   using two-stream models (Figure 11). For models that adopt other radiative transfer
572   algorithms it is best for the developers to examine their model against a benchmark
573   model such as 16-stream DISORT or two-stream models discussed in this work before
574   applying this correction.
575
576   It is important to note that although the errors of direct near-IR albedos are large for large
577   solar zenith angles, the absolute error in reflected shortwave flux is small (Figures 7 and
578   8) as the down-welling solar flux reaches snowpack decreases as solar zenith angle
579   increases (Figures 1(b)). However, such small biases in flux can be important to high
580   latitudes where the solar zenith angle remains large for many days in late winter and early
581   spring.
582

583   **7. Implementation of snow radiative transfer model in Earth system models**
584

585   ESMs often use broader band-averaged SSPs of snow and aerosols for computational
586   efficiency, rather than using brute-force integration of spectral solar properties across
587   narrower bands (per equation 11). Besides using different radiative transfer
588   approximations, SNICAR and dEdd-AD also adopt different methods to derive the band-
589   averaged SSPs of snow for different band schemes.
590

591   In SNICAR, snow solar properties are computed for 5 bands: one visible band (0.3 -
592   0.7μm), and four near-IR bands (0.7 - 1 μm, 1 – 1.2 μm, 1.2 – 1.5 μm, and 1.5 – 5 μm).
593   The solar properties of four subdivided near-IR bands are combined by fixed ratios to
594   compute the direct/diffuse near-IR snow properties. These two sets of ratios are derived
595   offline based on the incident solar spectra of typical of mid-latitude winter for clear and
596   cloudy-sky conditions clear sky and cloudy sky, respectively (Figure 1(a)).
597

598   The band-averaged SSPs of snow grains are computed following the Chandrasekhar
599   Mean approach (Thomas and Stamnes, 1999, their Equation 9.27; Flanner et al., 2007).

600   Specifically, spectral SSPs of snow grains are weighted into bands according to surface
601   incident solar flux typical of mid-latitude winter for clear and cloudy sky conditions. In
602   addition, the single-scattering albedo $\varpi(\lambda)$ of ice grains are also weighted by the
603   hemispheric albedo $\alpha(\lambda)$ of an optically thick snowpack:
604

605    $$\varpi(\bar{\lambda}) = \frac{\int_{\lambda_1}^{\lambda_2} \varpi(\lambda)F(\lambda)\alpha(\lambda)d\lambda}{\int_{\lambda_1}^{\lambda_2} F(\lambda)\alpha(\lambda)d\lambda} \tag{15a}$$

606    $$g(\bar{\lambda}) = \frac{\int_{\lambda_1}^{\lambda_2} g(\lambda)F(\lambda)d\lambda}{\int_{\lambda_1}^{\lambda_2} F(\lambda)\alpha(\lambda)d\lambda} \tag{15b}$$

607    $$\sigma_{ext}(\bar{\lambda}) = \frac{\int_{\lambda_1}^{\lambda_2} \sigma_{ext}(\lambda)F(\lambda)d\lambda}{\int_{\lambda_1}^{\lambda_2} F(\lambda)\alpha(\lambda)d\lambda} \tag{15c}$$

608
609   Two sets of snow band-averaged SSPs are generated for all grain radii, suitable for direct
610   and diffuse light, respectively. For each modeling step and band, SNICAR is called twice
611   to compute the direct and diffuse snow solar properties.
612
613   In dEdd-AD, the snow-covered sea ice properties are computed for 3 bands: one visible
614   band (0.3 – 07 µm), and two near-IR bands (0.7 – 1.19 µm and 1.19 – 5 µm). The solar
615   proprieties of these two near-IR bands are combined using ratios w_{nir1} and w_{nir2} for 0.7-1
616   .19 µm and 1.19-5 µm, depending on the fraction of direct near-IR flux f_{nidr}:
617

618    $$w_{nir1} = 0.67 + 0.11 * (1 - f_{nidr}) \tag{16a}$$

619    $$w_{nir2} = 1 - w_{nir1} \tag{16b}$$

620
621   The band SSPs of snow are derived by integrating the spectral SSPs and the spectral
622   surface solar irradiance measured in the Arctic under mostly clear sky.
623

624    $$\varpi(\bar{\lambda}) = \int_{\lambda_1}^{\lambda_2} \varpi(\lambda)F(\lambda)d\lambda \tag{17a}$$

625    $$g(\bar{\lambda}) = \int_{\lambda_1}^{\lambda_2} g(\lambda)F(\lambda)d\lambda \tag{17b}$$

626    $$\sigma_{ext}(\bar{\lambda}) = \int_{\lambda_1}^{\lambda_2} \sigma_{ext}(\lambda)F(\lambda)d\lambda \tag{17c}$$

627

628   In addition, the band-averaged single-scattering albedo $\varpi(\bar{\lambda})$ is also increased to $\varpi(\bar{\lambda})'$

629   until the band albedo computed using averaged SSPs matches the band albedo $\bar{\alpha}$ within

630   0.0001, where $\bar{\alpha}$ is:

631

632    $$\bar{\alpha} = \int_{\lambda_1}^{\lambda_2} \alpha(\lambda)F(\lambda)d\lambda \qquad (18)$$

633

634   dEdd-AD adopts this single set of band SSPs for both direct and diffuse computations. In

635   practice, the physical snow grain radius r is adjusted to a radiatively equivalent radius r_{eqv}

636   based on the fraction of direct flux in the near-IR band (f_{nidr}):

637

638    $$r_{eqv} = (f_{nidr} + 0.8(1 - f_{nidr}))r \qquad (19)$$

639

640   This r_{eqv} and the corresponding snow SSPs are then used in the radiative transfer

641   calculation. The computed direct and diffuse solar properties alone are less accurate,

642   while the combined all-sky broadband solar properties agree with SNICAR (Briegleb and

643   Light, 2007). As a result, for each modeling step and band, dEdd-AD radiative transfer

644   subroutine is called only once to compute both the direct and diffuse snow solar

645   properties simultaneously.

646

647   SNICAR and dEdd-AD also use different approaches to avoid numerical singularities. In

648   SNICAR, singularities occur when the denominator of term $C_n^{\pm}$ in equation (3) equals to

649   zero (i.e., $\gamma^2 - 1/\mu_0^2 = 0$), where γ is determined by the approximation method and SSPs

650   of snow, and μ_0 is the cosine of the solar zenith angle (Equations 23 and 24, Toon et al.,

651   1989). When such a singularity is detected, SNICAR will shift μ_0 by + 0.02 or -0.02 to

652   obtain physically realistic radiative properties. In the dEdd-AD algorithm, singularities

653   arise only when $\mu_0 = 0$ (Equation 4). Therefore, in practice, for $\mu_0 < 0.01$, dEdd-AD

654   computes the sea-ice solar properties for $\mu_0 = 0.01$ to avoid unphysical results.

655

656   **8. Discussion: a unified radiative transfer model for snow, sea ice, and land ice.**

657
658
659   Based on the inter-comparison of three two-stream algorithms and their implementations

660   in ESMs, we formulated the following surface shortwave radiative transfer

661 recommendations for an accurate, fast, and consistent treatment for snow on land, land
662 ice, and sea ice in ESMs:

663

664 First, the two-stream delta-Eddington adding-doubling algorithm by Briegleb and Light
665 (2007) is unsurpassed as a radiative transfer core. The evaluation in Section 5 shows that
666 this algorithm produces the least error for snow albedo and solar absorption within
667 snowpack, especially under overcast skies. This algorithm applies well to both uniformly
668 refractive media such as snow on land, and to non-uniformly refractive media, such as
669 bare/snow-covered/ponded sea ice and bare/snow-covered land ice. Numerical
670 singularities occur only rarely (when $\mu_0 = 0$) and are easily avoided in model
671 implementations. Among the three two-stream algorithms discussed here, dEdd-AD is
672 also the most efficient one as it takes only ~2/3 of the time of SNICAR and 2SD to
673 compute solar properties of multi-layer snowpacks.

674

675 Second, any two-stream cryospheric radiative transfer model can incorporate the
676 parameterization described in Section 6 to adjust the low bias of direct near-IR snow
677 albedo and high bias of direct near-IR solar absorption in snow, for solar zenith angles
678 larger than 75°. These biases are persistent across all two-stream algorithms discussed in
679 this work, and should be corrected for snow-covered surfaces. Alternatively, adopting a
680 4-stream approximation would reduce or eliminate such biases, though at considerable
681 expense in computational efficiency.

682

683 Third, a cryospheric radiative transfer model should prefer physically based
684 parameterizations that are extensible and convergent (e.g., with increasing spectral
685 resolution) for the band-averaged SSPs and size distribution of snow. Although the
686 treatments used in SNICAR and dEdd-AD are both practical since they both reproduce
687 the narrowband solar properties with carefully derived band-averaged inputs as discussed
688 in Section 7, the snow treatment used in SNICAR is more physically based and
689 reproducible since it does not rely on subjective adjustment and empirical coefficients as
690 used in dEdd-AD. Specifically, the empirical adjustment to snow grain radius
691 implemented in dEdd-AD may not always produce compensating errors. For example, in
692 snow containing light-absorbing impurities such adjustment may also lead to biases in
693 aerosol absorption since the albedo reduction caused by light-absorbing particles does not
694 linearly depend on snow grain radius (Dang et al., 2015). For further model development
695 incorporating non-spherical snow grain shapes (Dang et al., 2016; He et al., 2018ab),
696 such adjustment on grain radius may fail as well. Moreover, SNICAR computes the snow

697   properties for four near-IR bands, which helps capture the spectral variation of albedo

698   (Figure 1) and therefore better represents near-IR solar properties. It is also worth noting

699   that unlike the radiative core of dEdd-AD, SNICAR is actively maintained with

700   numerous modifications and updates in the past decade (e.g. Flanner et al., 2012; He et

701   al., 2018b). Snow radiative treatments that follow SNICAR conventions for SSPs may

702   take advantage of these updates. Note that any radiative core that follows SNICAR SSP

703   conventions must be called twice to compute diffuse and direct solar properties,

704   respectively.

705

706   Fourth, a surface cryospheric radiative transfer model should flexibly accommodate

707   coupled simulations with distinct atmospheric and surface spectral grids. Both the 5-band

708   scheme used in SNICAR and the 3-band scheme used in dEdd-AD separate the visible

709   from near-IR spectrum at 0.7 μm. This boundary aligns with the Community

710   Atmospheric Model's original radiation bands (CAM; Neale et al., 2012), though not

711   with the widely used Rapid Radiative Transfer Model (RRTMG; Iacono et al., 2008)

712   which places 0.7 μm squarely in the middle of a spectral band. A mismatch in spectral

713   boundaries between atmospheric and surface radiative transfer schemes can require an

714   ESM to unphysically apportion energy from the straddled spectral bin when coupling

715   fluxes between surface and atmosphere. The spectral grids of surface and atmosphere

716   radiation need not be identical so long as the coarser grid shares spectral boundaries with

717   the finer grid. In practice maintaining a portable cryospheric radiative module such as

718   SNICAR requires a complex offline toolchain (Mie solver, spectral refractive indices for

719   air, water, ice, and aerosols, spectral solar insolation for clear and cloudy skies) to

720   compute, integrate, and rebin SSPs. Aligned spectral boundaries between surface and

721   atmospheric would simplify the development of efficient and accurate radiative transfer

722   for the coupled Earth system.

723

724   Last, it is important to note that, although we only examine the performance of the dEdd-

725   AD for pure snow in this work, this algorithm can be applied to the surface solar

726   calculation of all cryospheric components with or without light-absorbing particles

727   present. First, Briegleb and Light (2007) proved its accuracy for simulating ponded/bare

728   sea-ice solar properties against observations and a Monte Carlo radiation model. Second,

729   In CESM and E3SM, the radiative transfer simulation of snow on land ice is carried out

730   by SNICAR with prescribed land ice albedo. Adopting dEdd-AD radiative core in

731   SNICAR will permit these ESMs to couple the snow and land ice as a non-uniformly

732   refractive column for more accurate solar computations since bare/snow-covered/ponded

733 land ice is physically similar to bare/snow-covered/ponded sea ice, and the latter is
734 already treated well by dEdd-AD radiative transfer core. Third, adding light-absorbing
735 particles in snow will not change our results qualitatively. Both dEdd-AD and SNICAR
736 simulate the impact of light-absorbing particles (black carbon and dust) on snow and/or
737 sea ice using self-consistent particle SSPs that follow the SNICAR convention (e.g.,
738 Flanner et al., 2007; Holland et al. 2012). These particles are assumed to be either
739 internally or externally mixed with snow crystals; the combined SSPs of mixtures (e.g.
740 Appendix A of Dang et al., 2015) are then used as the inputs for radiative transfer
741 calculation. The adoption of dEdd-AD radiative transfer algorithm in SNICAR, and the
742 implementation of SNICAR snow SSPs in dEdd-AD enables a consistent simulation of
743 the radiative effects of light-absorbing particles in the cryosphere across ESM
744 components.

746 In summary, this inter-comparison and evaluation has shown multiple ways that the solar
747 properties of cryospheric surfaces can be improved in the current generation of ESMs.
748 We have merged these findings into a hybrid model SNICAR-AD, which is primarily
749 composed of the radiative transfer scheme of dEdd-AD, 5-band snow/aerosol SSPs of
750 SNICAR, and the parameterization to correct for snow albedo biases when solar zenith
751 angle exceeds 75°. This hybrid model can be applied to snow on land, land ice, and sea
752 ice to produce consistent shortwave radiative properties for snow-covered surfaces across
753 the Earth system. With the evolving and further understanding of snow and aerosol
754 physics and chemistry, the adoption of this hybrid model will obviate the effort to modify
755 and maintain separate optical variable input files used for different model components.

757 SNICAR-AD is now implemented in both the sea-ice (MPAS-seaice) and land (ELM)
758 components of E3SM. More simulations and analyses are underway to examine its
759 impact on E3SM model performance and simulated climate. The results are however
760 beyond the scope of this work and will be thoroughly discussed in a future paper.

761 **9. Conclusions**

762 In this work, we aim to improve and unify the solar radiative transfer calculations for
763 snow on land and snow on sea ice in ESMs by evaluating the following two-stream
764 radiative transfer algorithms: the two-stream delta-Eddington adding-doubling algorithm
765 dEdd-AD implemented in sea-ice model Icepack/CICE/MPAS-seaice, the two-stream
766 delta-Eddington and two-stream delta-Hemispheric-Mean algorithms implemented in
767 snow model SNICAR, and a two-stream delta-Discrete-Ordinate algorithm. Among these
768 three models, the dEdd-AD produces the most accurate snow albedo and solar absorption

769   (Section 5). All two-stream models underestimate near-IR snow albedo and overestimate

770   near-IR absorption when solar zenith angles are larger than 75°, which can be adjusted by

771   a parameterization we developed (Section 6). We compared the implementations of

772   radiative transfer cores in SNICAR and dEdd-AD (Section 7) and recommended a

773   consistent and hybrid shortwave radiative model SNICAR-AD for snow-covered surfaces

774   across ESMs (Section 8). Improved treatment of surface cryospheric radiative properties

775   in the thermal infrared has recently been shown to remediate significant climate

776   simulation biases in Polar Regions (Huang et al., 2018). It is hoped that adoption of

777   improved and consistent treatments of solar radiative properties for snow-covered

778   surfaces as described in this study will further remediate simulation biases in snow-

779   covered regions.

780

781 **Data availability.** The data and models are available upon request to Cheng Dang
782 (cdang5@uci.edu). SNICAR and dEdd-AD radiative transfer core can be found at
783 https://github.com/E3SM-Project/E3SM.
784

785 **Competing interests.** The authors declare that they have no conflict of interest.
786

787 **Acknowledgments.** The authors thank Prof. Stephen G. Warren and Prof. Qiang Fu for
788 insightful discussions on radiative transfer algorithms. The authors thank Dr. Adrian
789 Turner for instructions on installing and running MPAS-seaice. The authors thank Dr.
790 David Bailey and one anonymous reviewer for their careful reading and insightful
791 suggestions. This research is supported as part of the Energy Exascale Earth System
792 Model (E3SM) project, funded by the U.S. Department of Energy, Office of Science,
793 Office of Biological and Environmental Research, with funding number DE-SC0012998.
794

795 **References**

796 Aoki, T., Kuchiki, K., Niwano, M., Kodama, Y., Hosaka, M. and Tanaka, T.: Physically
797 based snow albedo model for calculating broadband albedos and the solar heating
798 profile in snowpack for general circulation models. Journal of Geophysical Research,
799 116, D11114, https://doi.org/10.1029/2010JD015507, 2011.

800 Bøggild, C.E., Brandt, R.E., Brown, K.J. and Warren, S.G.: The ablation zone in
801 northeast Greenland: ice types, albedos and impurities. Journal of Glaciology, 56,
802 101-113, pp.101-113, https://doi.org/10.3189/002214310791190776, 2010.

803 Brandt, R.E., Warren, S.G., Worby, A.P. and Grenfell, T.C.: Surface albedo of the
804 Antarctic sea ice zone. Journal of Climate, 18(17), pp.3606-3622.
805 https://doi.org/10.1175/JCLI3489.1 2005.

806 Briegleb, P. and Light, B.: A Delta-Eddington mutiple scattering parameterization for
807 solar radiation in the sea ice component of the community climate system model,
808 2007.

809 Dang, C. and Hegg, D.A.: Quantifying light absorption by organic carbon in Western
810 North American snow by serial chemical extractions. Journal of Geophysical
811 Research, 119(17), pp.10-247. https://doi.org/10.1002/2014JD022156, 2014.

812 Dang, C., Fu, Q. and Warren, S.G., 2016. Effect of snow grain shape on snow albedo.
813 Journal of the Atmospheric Sciences, 73(9), pp.3573-3583.
814 https://doi.org/10.1175/JAS-D-15-0276.1, 2016.

815 Dang, C., Brandt, R.E. and Warren, S.G.: Parameterizations for narrowband and
816 broadband albedo of pure snow and snow containing mineral dust and black carbon.
817 Journal of Geophysical Research: Atmospheres, 120(11), pp.5446-5468,
818 https://doi.org/10.1002/2014JD022646, 2015.

819 Dang, C., Warren, S.G., Fu, Q., Doherty, S.J., Sturm, M. and Su, J.: Measurements of
820 light-absorbing particles in snow across the Arctic, North America, and China:
821 Effects on surface albedo. Journal of Geophysical Research: Atmospheres, 122(19),
822 pp.10-149. https://doi.org/10.1002/2017JD027070, 2017.

823 Doherty, S.J., Hegg, D.A., Johnson, J.E., Quinn, P.K., Schwarz, J.P., Dang, C. and
824   Warren, S.G.: Causes of variability in light absorption by particles in snow at sites in
825   Idaho and Utah. Journal of Geophysical Research: Atmospheres, 121(9), pp.4751-
826   4768. https://doi.org/10.1002/2015JD024375, 2016.

827 Doherty, S.J., Warren, S.G., Grenfell, T.C., Clarke, A.D. and Brandt, R.E.: Light-
828   absorbing impurities in Arctic snow. Atmospheric Chemistry and Physics. 10(23),
829   pp.11647-11680. https://doi.org/10.5194/acp-10-11647-2010, 2010.

830 Doherty, S.J., Dang, C., Hegg, D.A., Zhang, R. and Warren, S.G.: Black carbon and other
831   light-absorbing particles in snow of central North America. Journal of Geophysical
832   Research: Atmospheres, 119(22), pp.12-807, https://doi.org/10.1002/2014JD022350,
833   2014.

834 Flanner, M.G. and Zender, C.S.: Snowpack radiative heating: Influence on Tibetan
835   Plateau climate. Geophysical Research Letters, 32(6).
836   https://doi.org/10.1029/2004GL022076, 2005.

837 Flanner, M.G., Zender, C.S., Randerson, J.T. and Rasch, P.J.: Present-day climate forcing
838   and response from black carbon in snow. Journal of Geophysical Research:
839   Atmospheres, 112(D11). https://doi.org/10.1029/2006JD008003, 2007.

840 Flanner, M.G., Liu, X., Zhou, C., Penner, J.E. and Jiao, C.: Enhanced solar energy
841   absorption by internally-mixed black carbon in snow grains. Atmospheric Chemistry
842   and Physics, 12(10), pp.4699-4721. https://doi.org/10.5194/acp-12-4699-2012, 2012.

843 Gardner, A.S. and Sharp, M.J.: A review of snow and ice albedo and the development of
844   a new physically based broadband albedo parameterization. Journal of Geophysical
845   Research: Earth Surface, 115(F1). https://doi.org/10.1029/2009JF001444, 2010.

846 Grenfell, T.C., Neshyba, S.P. and Warren, S.G.: Representation of a nonspherical ice
847   particle by a collection of independent spheres for scattering and absorption of
848   radiation: 3. Hollow columns and plates. Journal of Geophysical Research:
849   Atmospheres, 110(D17). https://doi.org/10.1029/2005JD005811, 2005.

850 He, C., Liou, K.N., Takano, Y., Yang, P., Qi, L. and Chen, F.: Impact of grain shape and
851   multiple black carbon internal mixing on snow albedo: Parameterization and radiative
852   effect analysis. Journal of Geophysical Research: Atmospheres, 123(2), pp.1253-
853   1268. https://doi.org/10.1002/2017JD027752, 2018a.

854 He, C., Flanner, M.G., Chen, F., Barlage, M., Liou, K.N., Kang, S., Ming, J. and Qian,
855   Y.: Black carbon-induced snow albedo reduction over the Tibetan Plateau:
856   uncertainties from snow grain shape and aerosol–snow mixing state based on an
857   updated SNICAR model. Atmospheric Chemistry and Physics, 18, pp.11507-11527.
858   https://doi.org/10.5194/acp-18-11507-2018, 2018b.

859 He, C., Takano, Y., Liou, K.N., Yang, P., Li, Q. and Chen, F.: Impact of Snow Grain
860   Shape and Black Carbon–Snow Internal Mixing on Snow Optical Properties:
861   Parameterizations for Climate Models. Journal of Climate, 30(24), pp.10019-10036.
862   https://doi.org/10.1175/JCLI-D-17-0300.1, 2017.

863 Holland, M.M., Bailey, D.A., Briegleb, B.P., Light, B. and Hunke, E.: Improved sea ice
864   shortwave radiation physics in CCSM4: The impact of melt ponds and aerosols on

865   Arctic sea ice. Journal of Climate, 25(5), pp.1413-1430. https://doi.org/10.1175/JCLI-
866   D-11-00078.1, 2012.

867   Huang, X., Chen, X., Flanner, M., Yang, P., Feldman, D. and Kuo, C.: Improved
868   representation of surface spectral emissivity in a global climate model and its impact
869   on simulated climate. Journal of Climate, 31(9), pp.3711-3727.
870   https://doi.org/10.1175/JCLI-D-17-0125.1, 2018.

871   Hunke, E. C., Lipscomb, W. H., Turner, A. K., Jeffery, N., and Elliott, S.: CICE: the Los
872   Alamos Sea Ice Model Documentation and Software User's Manual Version 4.1 LA-
873   CC-06-012. T-3 Fluid Dynamics Group, Los Alamos National Laboratory 675. 2010.

874   Iacono, M.J., Delamere, J.S., Mlawer, E.J., Shephard, M.W., Clough, S.A. and Collins,
875   W.D.: Radiative forcing by long‐lived greenhouse gases: Calculations with the AER
876   radiative transfer models. Journal of Geophysical Research: Atmospheres, 113(D13),
877   https://doi.org/10.1029/2008JD009944, 2008.

878   Jin, Z. and Stamnes, K.: Radiative transfer in nonuniformly refracting layered media:
879   atmosphere–ocean system. Applied Optics, 33(3), pp.431-442.
880   https://doi.org/10.1364/AO.33.000431, 1994.

881   Kuipers Munneke, P., Van den Broeke, M.R., Lenaerts, J.T.M., Flanner, M.G., Gardner,
882   A.S. and Van de Berg, W.J.: A new albedo parameterization for use in climate
883   models over the Antarctic ice sheet. Journal of Geophysical Research: Atmospheres,
884   116(D5). https://doi.org/10.1029/2010JD015113, 2011.

885   Lee, W.L. and Liou, K.N.: A coupled atmosphere–ocean radiative transfer system using
886   the analytic four-stream approximation. Journal of the Atmospheric Sciences, 64(10),
887   pp.3681-3694. https://doi.org/10.1175/JAS4004.1, 2007.

888   Liang, S., Fang, H., Chen, M., Shuey, C.J., Walthall, C., Daughtry, C., Morisette, J.,
889   Schaaf, C. and Strahler, A.: Validating MODIS land surface reflectance and albedo
890   products: Methods and preliminary results. Remote sensing of environment, 83(1-2),
891   pp.149-162. https://doi.org/10.1016/S0034-4257(02)00092-5, 2002.

892   Light, B., Grenfell, T. C. and Perovich, D.K.: Transmission and absorption of solar
893   radiation by Arctic sea ice during the melt season. Journal of Geophysical Research:
894   Oceans 113, no. C3, https://doi.org/10.1029/2006JC003977, 2008.

895   Light, B., Perovich, D.K., Webster M.A., Polashenski, C., and Dadic, R.: Optical
896   properties of melting first-year Arctic sea ice. Journal of Geophysical Research:
897   Oceans 120, no. 11: 7657-7675, https://doi.org/10.1002/2015JC011163, 2015.

898   Marshall, S. and Oglesby, R.J.: An improved snow hydrology for GCMs. Part 1: Snow
899   cover fraction, albedo, grain size, and age. Climate Dynamics, 10(1-2), pp.21-37.
900   https://doi.org/10.1007/BF00210334, 1994.

901   Marshall, S.E.: A Physical Parameterization of Snow Albedo for Use in Climate Models,
902   NCAR Cooperative Thesis 123, National Center for Atmospheric Research,
903   Boulder, CO, 175 pp. 1989.

904 Matzl, M. and Schneebeli, M.: Measuring specific surface area of snow by near-infrared
905   photography. Journal of Glaciology, 52(179), pp.558-564.
906   https://doi.org/10.3189/172756506781828412, 2006.

907 Matzl, M. and Schneebeli, M.: Stereological measurement of the specific surface area of
908   seasonal snow types: Comparison to other methods, and implications for mm-scale
909   vertical profiling. Cold Regions Science and Technology, 64(1), pp.1-8.
910   https://doi.org/10.1016/j.coldregions.2010.06.006, 2010.

911 Meador, W.E. and Weaver, W.R.: Two-stream approximations to radiative transfer in
912   planetary atmospheres: A unified description of existing methods and a new
913   improvement. Journal of the Atmospheric Sciences, 37(3), pp.630-643.
914   https://doi.org/10.1175/1520-0469(1980)037<0630:TSATRT>2.0.CO;2, 1980.

915 Mlawer, E.J. and Clough, S.A.: On the extension of rapid radiative transfer model to the
916   shortwave region. In Proceedings of the 6th Atmospheric Radiation Measurement
917   (ARM) Science Team Meeting, US Department of Energy, CONF-9603149, 223–
918   226. 1997.

919 Neale, Richard B., Chen, C.-C., Gettelman, A., Lauritzen, P. H., Park, S., Williamson, D.
920   L., Conley, A. J., Garcia, R., Kinnison, D., Lamarque, J. F., and Marsh, D.:
921   Description of the NCAR community atmosphere model (CAM 5.0). NCAR Tech.
922   Note NCAR/TN-486+ STR 1, no. 1: 1-12. 2010.

923 Neshyba, S.P., Grenfell, T.C. and Warren, S.G.: Representation of a nonspherical ice
924   particle by a collection of independent spheres for scattering and absorption of
925   radiation: 2. Hexagonal columns and plates. Journal of Geophysical Research:
926   Atmospheres, 108(D15). https://doi.org/10.1029/2002JD003302, 2003.

927 Perovich, D. K.: The optical properties of sea ice (No. MONO-96-1). COLD REGIONS
928   RESEARCH AND ENGINEERING LAB HANOVER NH. 1996.

929 Stamnes, K., Tsay, S.C., Wiscombe, W. and Jayaweera, K.: Numerically stable algorithm
930   for discrete-ordinate-method radiative transfer in multiple scattering and emitting
931   layered media. Applied optics, 27(12), pp.2502-2509.
932   https://doi.org/10.1364/AO.27.002502, 1988.

933 Thomas, G.E. and K. Stamnes (1999), Radiative transfer in the atmosphere and ocean.
934   Cambridge University Press.

935 Toon, O. B., McKay, C. P., Ackerman, T. P., and Santhanam, K.: Rapid calculation of
936   radiative heating rates and photodissociation rates in inhomogeneous multiple
937   scattering atmospheres, J. Geophys. Res., 94(D13), 16,287–16,301.
938   https://doi.org/10.1029/JD094iD13p16287, 1989.

939 Turner, A.K., Lipscomb, W.H., Hunke, E.C., Jacobsen, D.W., Jeffery, N., Ringler, T.D.
940   and Wolfe, J.D.: MPAS-Seaice: a new variable resolution sea-ice model. J. Adv.
941   Model Earth Sy., in preparation., 2018.

942 Wang, X., Doherty, S.J. and Huang, J.: Black carbon and other light-absorbing
943   impurities in snow across Northern China. Journal of Geophysical Research:
944   Atmospheres, 118(3), pp.1471-1492. https://doi.org/10.1029/2012JD018291, 2013.

945   Warren, S. G.: Optical properties of snow. Reviews of Geophysics 20, no. 1: 67-89.
946   https://doi.org/10.1029/RG020i001p00067,1982.

947   Warren, S.G. and Wiscombe, W.J.: A model for the spectral albedo of snow. II: Snow
948   containing atmospheric aerosols. Journal of the Atmospheric Sciences, 37(12),
949   pp.2734-2745.https://doi.org/10.1175/1520-
950   0469(1980)037<2734:AMFTSA>2.0.CO;2, 1980

951   Warren, S.G. and Brandt, R.E.: Optical constants of ice from the ultraviolet to the
952   microwave: A revised compilation. Journal of Geophysical Research: Atmospheres,
953   113(D14). https://doi.org/10.1029/2007JD009744, 2008.

954   Warren, S.G. and Wiscombe, W.J.: Dirty snow after nuclear war. Nature, 313(6002),
955   p.467. https://doi.org/10.1038/313467a0, 1985.

956   Wiscombe, W. J.: The delta-Eddington approximation for a vertically inhomogeneous
957   atmosphere, NCAR Tech. Note TN-140_STR [NTIS P6270618]. 1977.

958   Wiscombe, W.J.: Improved Mie scattering algorithms. Applied optics, 19(9), pp.1505-
959   1509. https://doi.org/10.1364/AO.19.001505,1980.

960   Wiscombe, W.J. and Warren, S.G.: A model for the spectral albedo of snow. I: Pure
961   snow. Journal of the Atmospheric Sciences, 37(12), pp.2712-2733.
962   https://doi.org/10.1175/1520-0469(1980)037<2712:AMFTSA>2.0.CO;2, 1980.

963   Zender, C.S.: Global climatology of abundance and solar absorption of oxygen collision
964   complexes. Journal of Geophysical Research: Atmospheres, 104(D20), pp.24471-
965   24484. https://doi.org/10.1029/1999JD900797, 1999.

966   Zender, C.S., Bush, B., Pope, S.K., Bucholtz, A., Collins, W.D., Kiehl, J.T., Valero, F.P.
967   and Vitko Jr, J.: Atmospheric absorption during the atmospheric radiation
968   measurement (ARM) enhanced shortwave experiment (ARESE). Journal of
969   Geophysical Research: Atmospheres, 102(D25), pp.29901-29915.
970   https://doi.org/10.1029/97JD01781, 1997.

971

972 Figure 1. The spectral albedo of pure snow computed using 16-stream DISORT,
973 SNICAR, dEdd-AD, and 2SD models, for clear-sky (direct beam at solar zenith angle
974 60°) and cloudy-sky conditions in the left and right panels, respectively. The top panels
975 show spectral albedo. The middle panels show the difference ($\delta\alpha = \alpha_2 - \alpha_{16}$) in spectral
976 albedos computed using the two-stream model (α_2) and 16-stream DISORT (α_{16}). The
977 bottom panels show the difference of reflected spectral flux given $\delta\alpha$. The snowpack is
978 set to semi-infinite deep with grain radius of 100 μm.
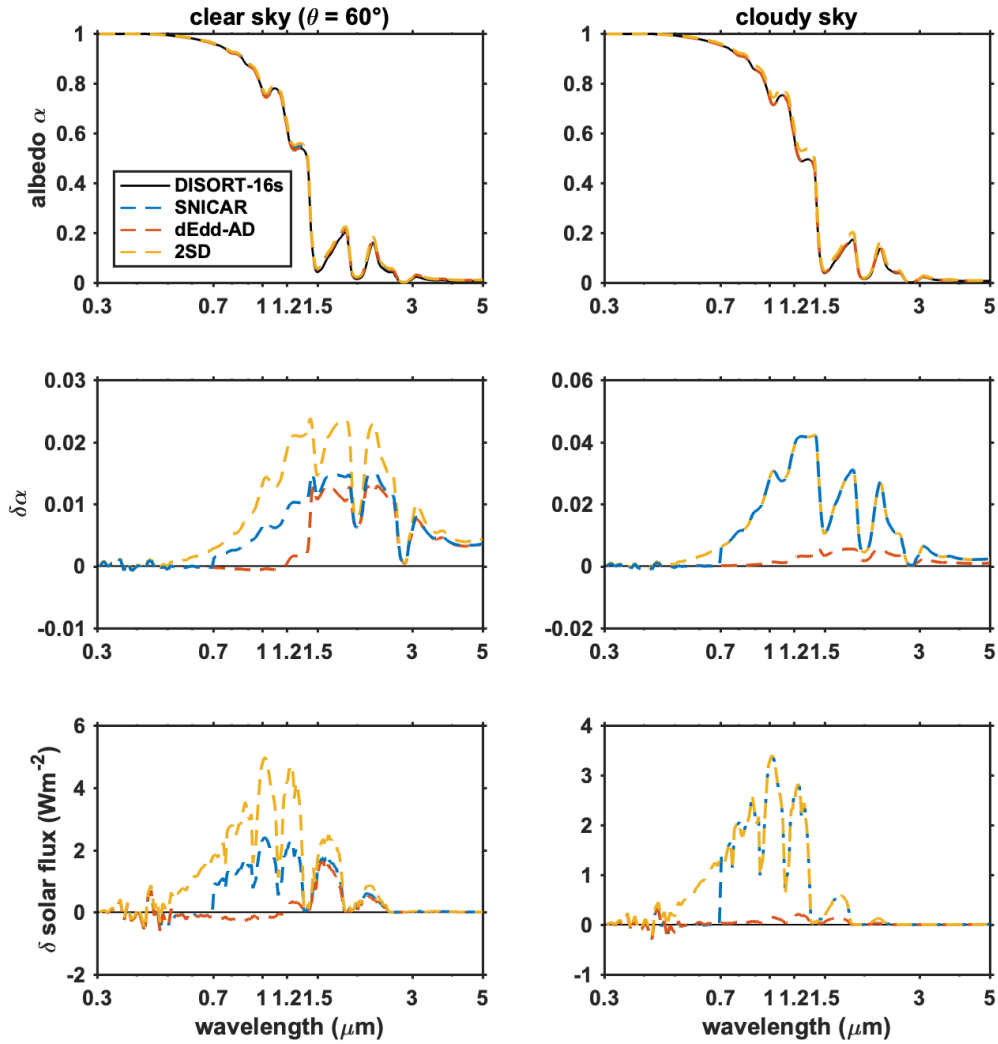
979
980
981
982

983   Figure 2. Spectral and total down-welling solar flux at surface computed using SWNB2
984   for (a) standard clear-sky and cloudy-sky atmospheric profiles of mid-latitude winter
985   assuming solar zenith angle is 60° at the top of the atmosphere, and for (b) standard clear
986   sky profiles of mid-latitude and sub-Arctic winter with different incident solar zenith
987   angles.
988
989
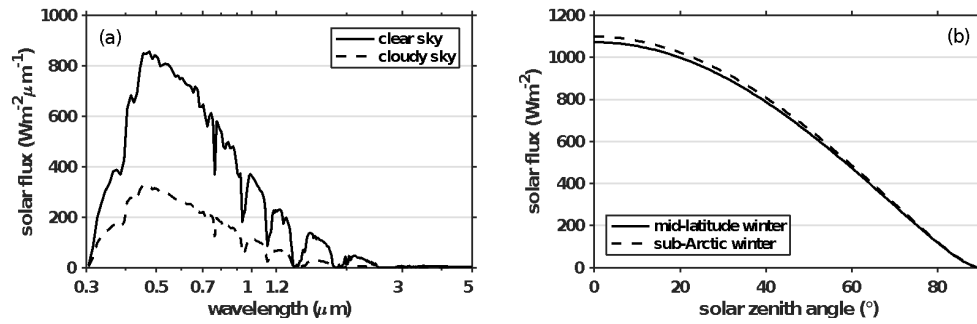
990
991
992

993 Figure 3. The difference in direct snow albedo ($\delta\alpha = \alpha_2 - \alpha_{16}$) computed using two-stream
994 models (α_2) and using 16-stream DISORT model (α_{16}), for various snow depths and solar
995 zenith angles, with snow grain radius of 100 μm. From the top to the bottom rows are
996 results of two-stream models SNICAR, dEdd-AD, and 2SD. From the left to the right
997 columns are albedo differences of all-wave, visible, near-IR bands.

998
999
1000
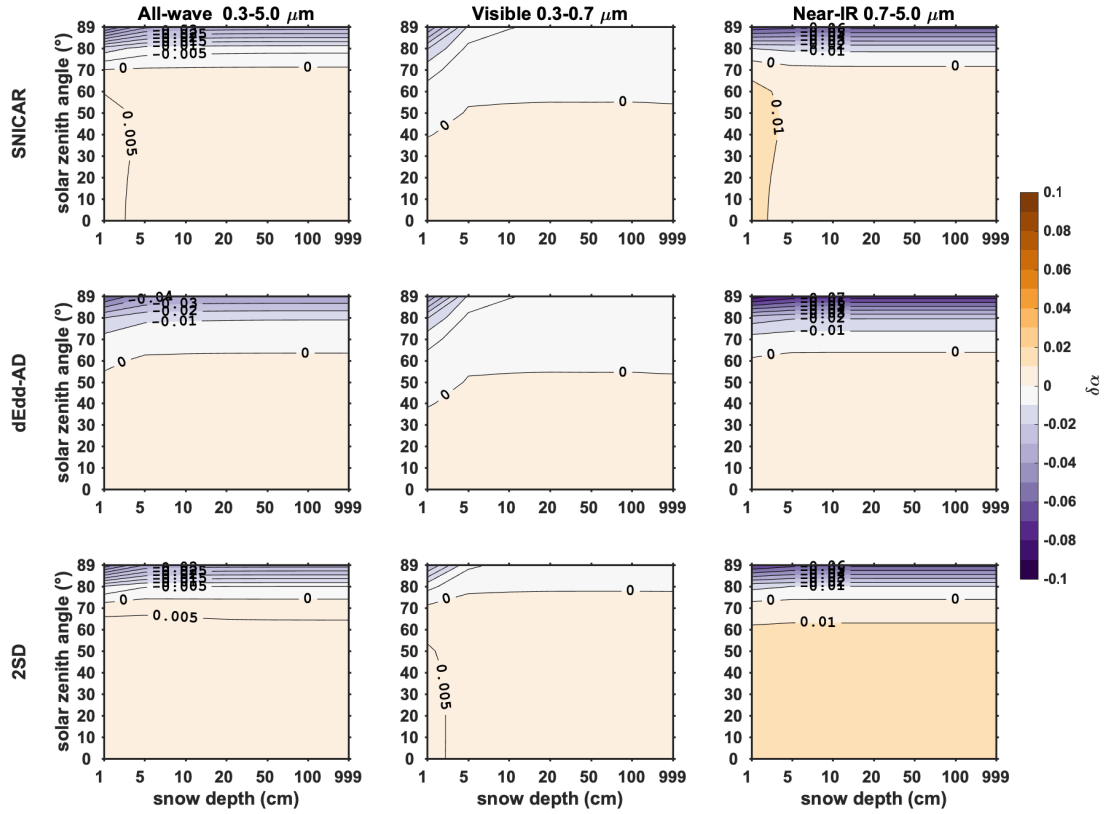
none
Figure 4. The difference in direct snow albedo ($\delta\alpha = \alpha_2 - \alpha_{16}$) computed using two-stream models (α_2) and using 16-stream DISORT model (α_{16}), for various snow depths and solar zenith angles, with snow grain radius of 1000 μm.
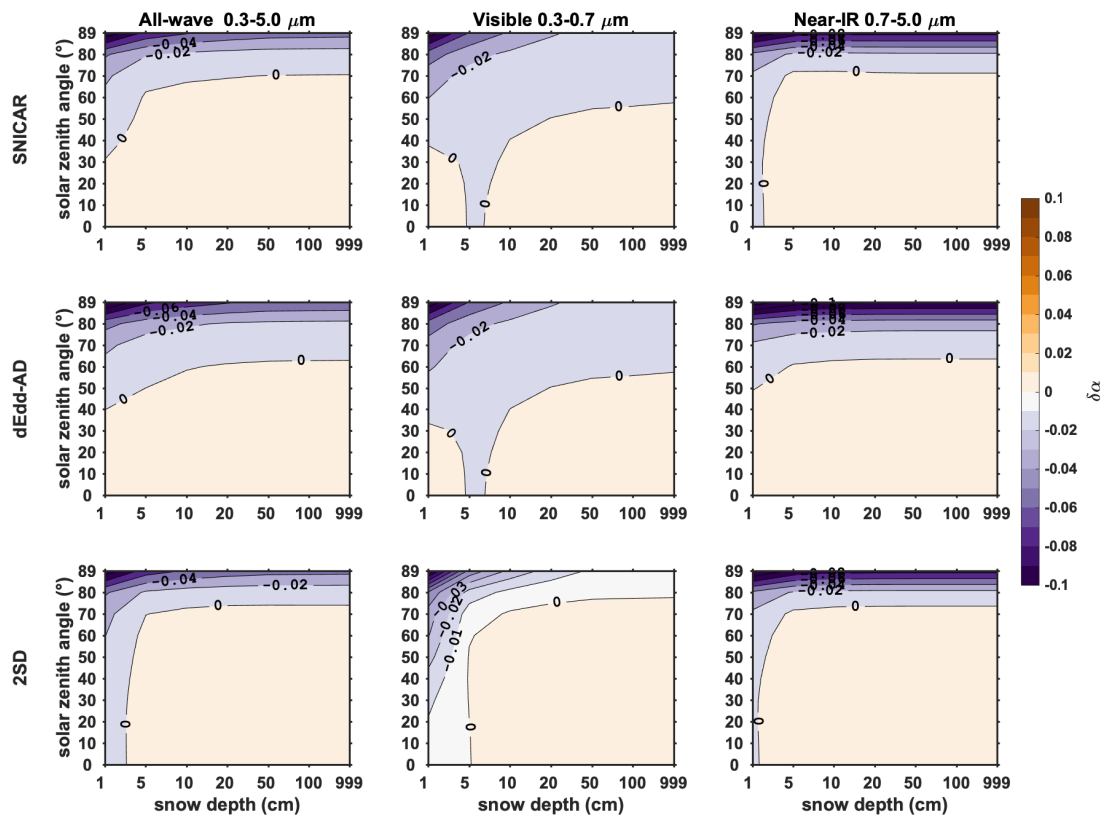
Figure 5. The difference in direct snow albedo ($\delta\alpha = \alpha_2 - \alpha_{16}$) computed using two-stream models (α_2) and using 16-stream DISORT model (α_{16}), for various snow depths and snow grain radii, with solar zenith angle of 60°.
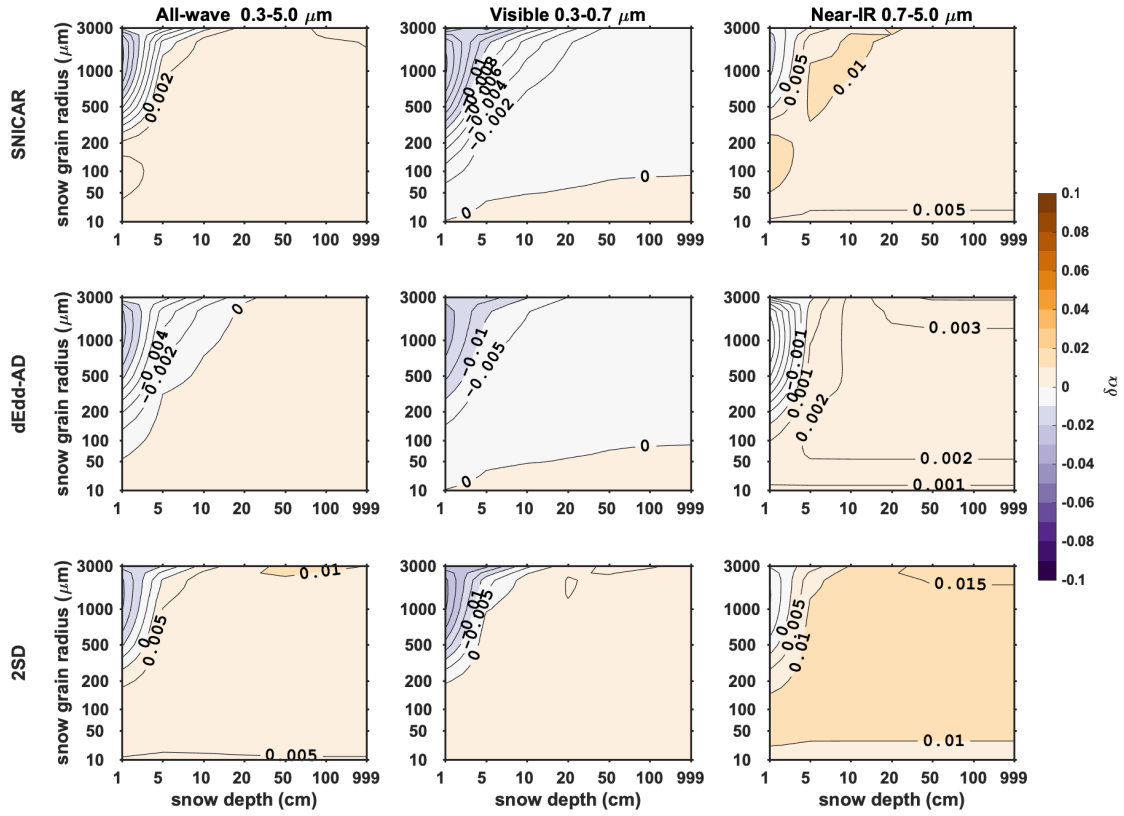
Figure 6. The difference in diffuse snow albedo ($\delta\alpha = \alpha_2 - \alpha_{16}$) computed using two-
stream models (α_2) and using 16-stream DISORT model (α_{16}), for various snow depths
and snow grain radii, with solar zenith angle of 60° at the top of the atmosphere.
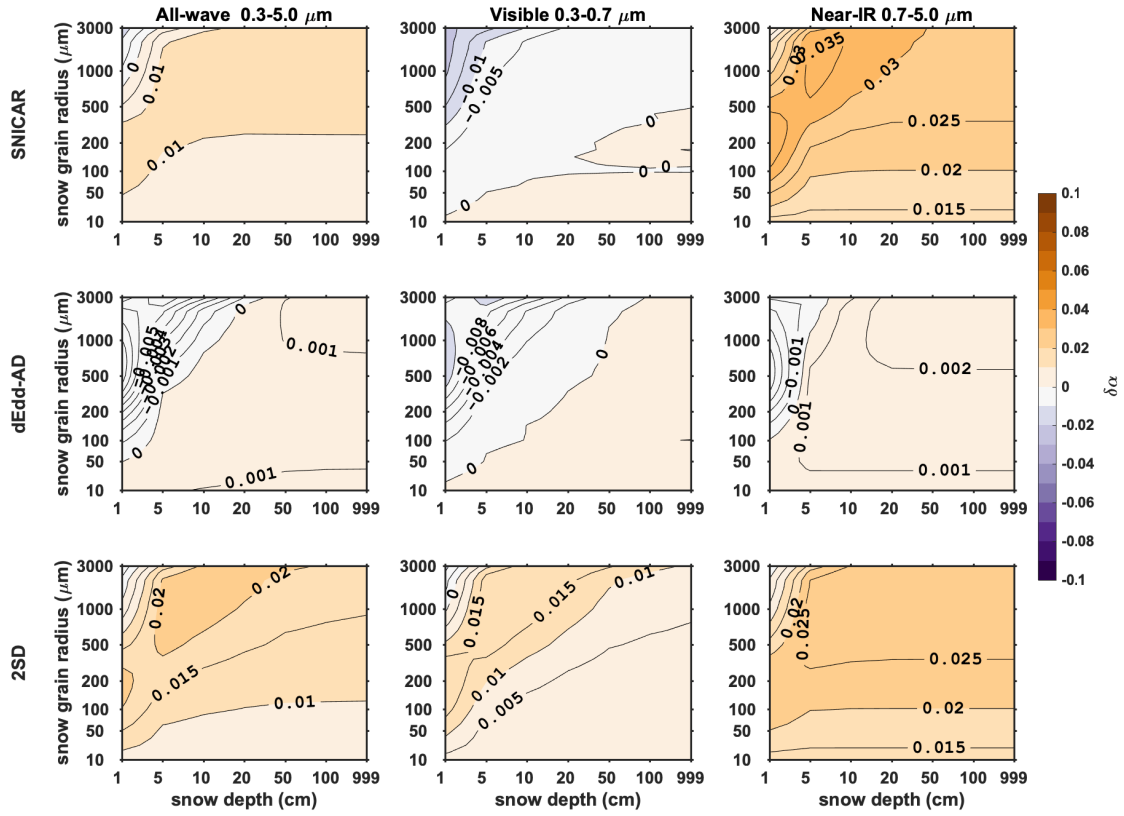
1019   Figure 7. Error in reflected direct solar flux given albedo errors shown in Figure 3.
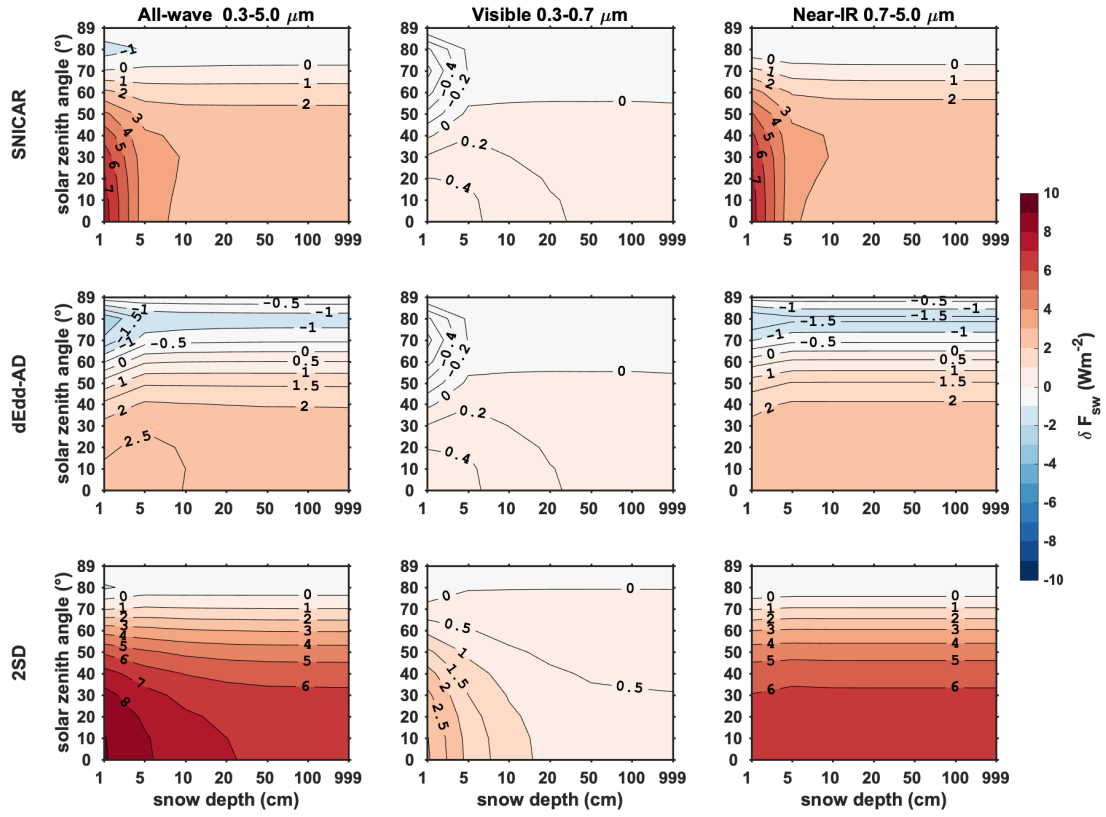
1020
1021

1022   Figure 8. Error in reflected direct solar flux given albedo errors shown in Figure 4.
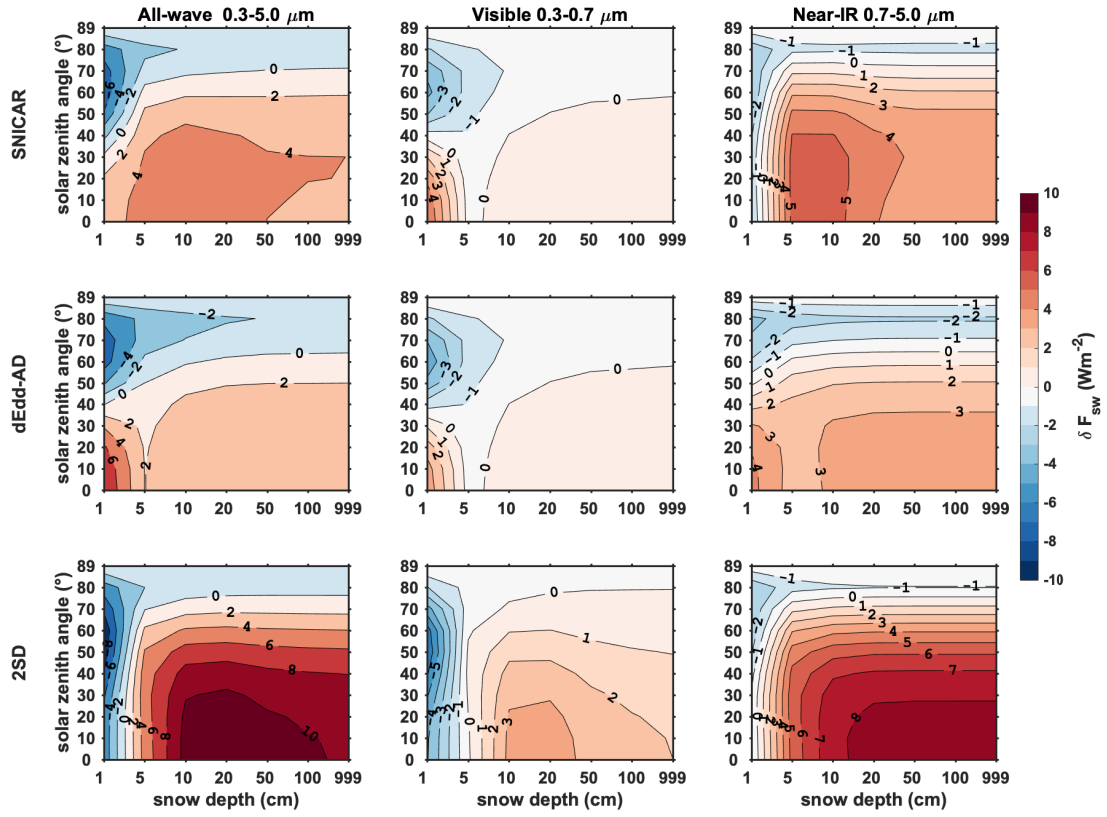
1023
1024
1025

1026   Figure 9. Error in reflected diffuse solar flux given albedo errors shown in Figure 6.
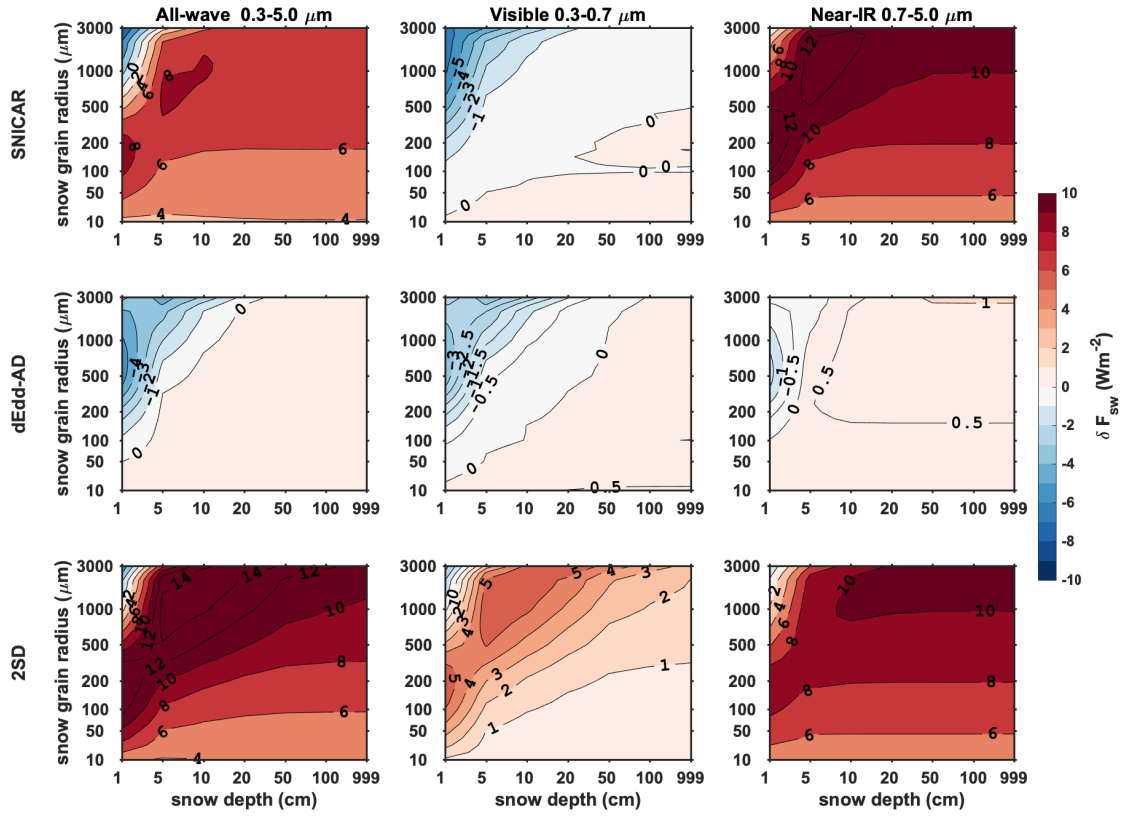
1027
1028
1029

Figure 10. Comparison of light-absorption profiles derived from two-stream models and 16-stream DISORT. The left-most column shows fractional band absorptions computed using 16-stream DISORT. The right three panels show the errors of all-wave, visible, and near-IR fractional absorptions calculated using two-stream models. The top and bottom panels are for clear-sky and cloudy-sky conditions (solar zenith angle of 60°), respectively. The snowpack is 10 cm deep and is divided evenly into five 2-cm thick layers, for new snow (r = 100 μm) and old snow (r = 1000 μm). The layers 1-4 represent the top four snow layers (top 8 cm), and layer 5 represents underlying ground with albedo of 0.25.
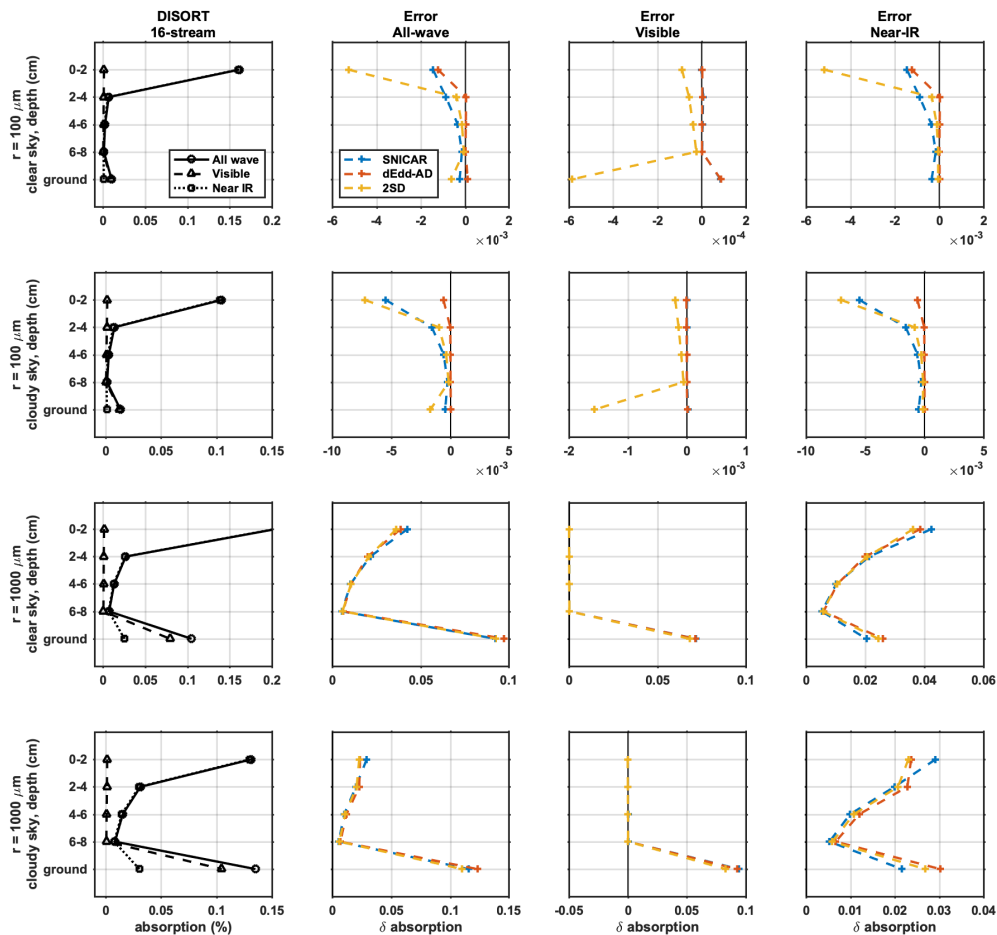
1041
1042 Figure 11. (a) Direct near-IR snow albedo and (b) near-IR fractional absorption by top 2-
1043 cm snow of a 2-m thick snowpack, for solar zenith angles larger than 70° and snow grain
1044 radii of 100 μm and 1000 μm. (c) The ratios of near-IR albedo computed using CICE to
1045 that computed using 16-stream DISORT for different solar zenith angles. These ratios are
1046 parameterized as linear functions of the logarithmic of snow grain radius. The slopes and
1047 y-intercepts are shown in (d). The black dashed curves in figures (c) and (d) are fitting
1048 values computed using parameterization discussed in Section 5.
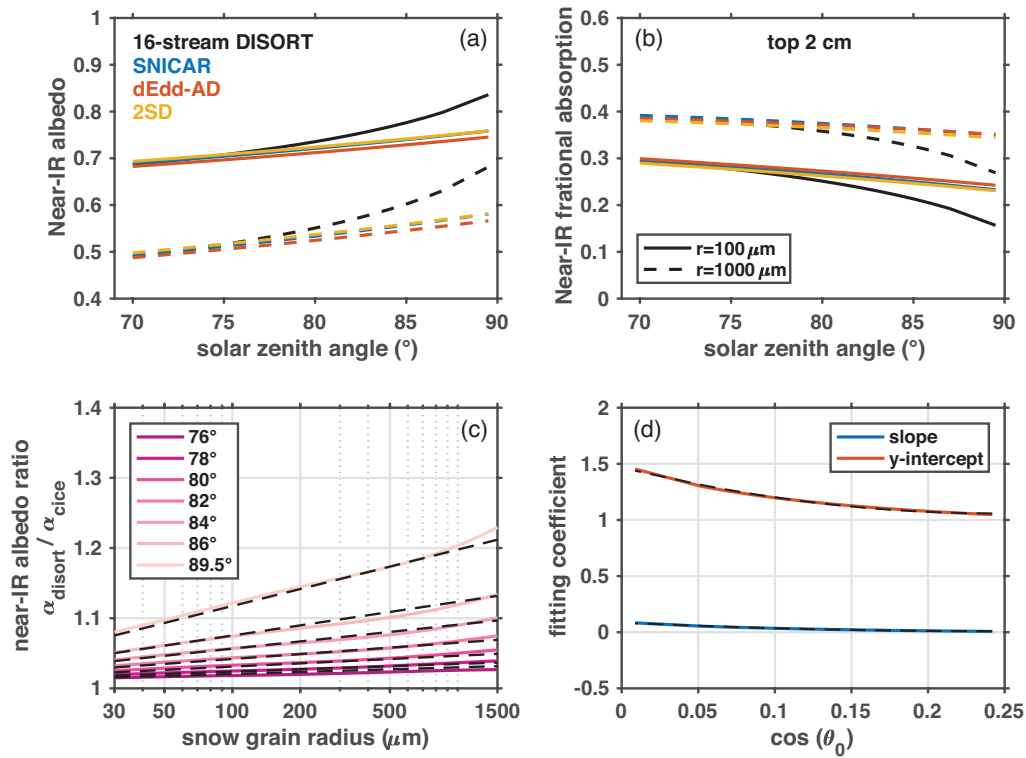
1049
1050
1051
1052

1053 Figure 12. Error in semi-infinite snow albedo computed using dEdd-AD before (top row)
1054 and after (bottom row) incorporating corrections for near-IR albedo, for different solar
1055 zenith angles and snow grain radii.
1056
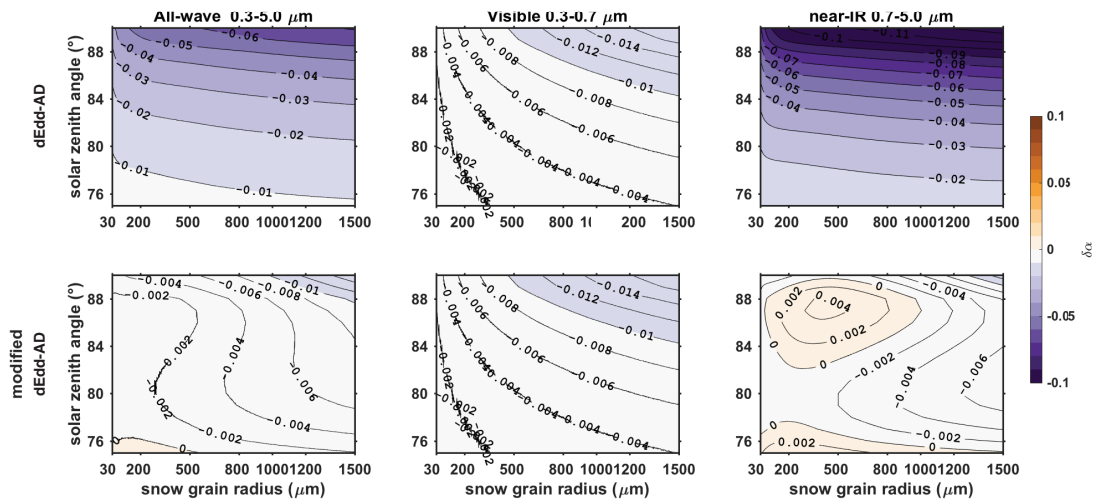
1057
1058
1059
1060

   Table 1. Acronyms used in this paper and their references.

ESM/ESMs	Earth System Models	
E3SM	Energy Exscale Earth System Model	Global climate model, previously know as ACME, htttps://e3sm.org/
CESM	Community Earth System Model	Global climate model, http://www.cesm.ucar.edu/
CCSM	Community Climate System Model	Global climate model, http://www.cesm.ucar.edu/models/ccsm4.0/
RACMO	Regional Atmospheric Climate Model	Regional model, https://www.projects.science.uu.nl/iceclimate/models/racmo.php
CAM	Community Atmospheric Model	Atmospheric model, Neale et al., 2012
ELM	E3SM land model	Land model of E3SM, https://e3sm.org/model/e3sm-model-description/v1-description/
CLM	Community land model	Land model of CESM, http://www.cesm.ucar.edu/models/clm/
MPAS-seaice	Model for Prediction Across Scales Sea Ice	Sea-ice model of E3SM, Turner et al., 2018
CICE	Los Almos Sea Ice Model	Sea-ice model of CESM, Hunke et al., 2010
RRTM	Rapid Radiative Transfer Model	Standalone column radiative transfer model, Mlawer and Clough, 1997, http://rtweb.aer.com/rrtm_frame.html
RRTMG	Rapid Radiative Transfer Model for GCM components	Modified RRTM for GCM application, Iacono et al., 2008, http://rtweb.aer.com/rrtm_frame.html
DISORT	DIScrete-Odinate Radiative Transfer model	Standalone column radiative transfer model, http://lllab.phy.stevens.edu/disort/, Stamnes et al., 1988
SWNB2	Shortwave Narrowband Model	Standalone column radiative transfer model, Zender et al., 1997; Zender, 1999
SNICAR	SNow ICe and Aerosol Radiative module	Snow module used in ELM and CLM, Flanner and Zender, 2005; Toon et al., 1989

dEdd-AD	Two-stream delta-Eddington Adding-Doubling radiative transfer algorithm	Sea-ice radiative transfer core in MPAS-seaice and CICE, Briegleb and Light, 2007
2SD	Two-Stream Discrete ordinate radiative transfer algorithm	Radiative transfer algorithm tested in this work, Jin and Stamnes, 1994
SNICAR-AD	SNICAR – Adding Doubling	Hybrid snow/sea-ice radiative transfer model, Section 8
SSP/SSPs	Single-Scattering Properties	Single-scattering albedo ϖ, asymmetry factor g, extinction coefficient σ_{ext}
near-IR	Near Infrared band	Wavelengths of 0.7 - 5 μm

1064
1065

1066
1067 Table 2. Two-stream radiative transfer algorithms evaluated in this work, including
1068 algorithms that are currently implemented in Earth System Model CESM and E3SM.
1069
1070

ESM Component	Land	Sea Ice	
Model	SNICAR	dEdd-AD	2SD
Radiative transfer approximation	two-stream δ-Eddington (visible) δ-Hemispheric-mean (near-IR)	two-stream δ-Eddington	two-stream δ-Discrete-ordinate
Treatment for multi-layered media	matrix inversion	adding-doubling	matrix inversion
Fresnel reflection/refraction	no	yes	yes
Number of bands implemented in ESMs	5 bands (1 visible, 4 near-IR)	3 bands (1 visible, 2 near-IR)	
Applies to	snow	bare/ponded/snow-covered sea ice, and snow	bare/ponded/snow-covered sea ice, and snow

1071